

Model-Based Analysis of Excitatory Lateral Connections in the Visual Cortex

PÉTER BUZÁS,^{1,2*} KRISZTINA KOVÁCS,¹ ALEX S. FERECSKÓ,¹
JULIAN M.L. BUDD,³ ULF T. EYSEL,¹ AND ZOLTÁN F. KISVÁRDAY^{1,4}

¹Department of Neurophysiology, Ruhr-Universität Bochum, Bochum 44780, Germany
²National Vision Research Institute of Australia and Department of Optometry and Vision Sciences, University of Melbourne, Carlton 3053, Australia

³Department of Informatics, University of Sussex, Brighton BN1 9RH, UK

⁴Department of Anatomy, Histology and Embryology, University of Debrecen, Debrecen 4012, Hungary

ABSTRACT

Excitatory lateral connections within the primary visual cortex are thought to link neurons with similar receptive field properties. Here we studied whether this rule can predict the distribution of excitatory connections in relation to cortical location and orientation preference in the cat visual cortex. To this end, we obtained orientation maps of areas 17 or 18 using optical imaging and injected anatomical tracers into these regions. The distribution of labeled axonal boutons originating from large populations of excitatory neurons was then analyzed and compared with that of individual pyramidal or spiny stellate cells. We demonstrate that the connection patterns of populations of nearby neurons can be reasonably predicted by Gaussian and von Mises distributions as a function of cortical location and orientation, respectively. The connections were best described by superposition of two components: a spatially extended, orientation-specific and a local, orientation-invariant component. We then fitted the same model to the connections of single cells. The composite pattern of nine excitatory neurons (obtained from seven different animals) was consistent with the assumptions of the model. However, model fits to single cell axonal connections were often poorer and their estimated spatial and orientation tuning functions were highly variable. We conclude that the intrinsic excitatory network is biased to similar cortical locations and orientations but it is composed of neurons showing significant deviations from the population connectivity rule. *J. Comp. Neurol.* 499:861–881, 2006. © 2006 Wiley-Liss, Inc.

Indexing terms: horizontal connections; pyramidal neurons; spiny stellate neurons; orientation map; von Mises distribution

The majority of synapses in the neocortex are provided by cortico-cortical connections (Peters and Payne, 1993; Ahmed et al., 1994). Of these, intrinsic lateral connections, i.e., those running parallel to the cortical surface within a cortical area, are thought to be important in the formation of large-scale functional maps observed in sensory cortices (Mitchison and Crick, 1982; Gilbert and Wiesel, 1983; Xing and Gerstein, 1996; Adorján et al., 1999; Shouval et al., 2000; Ernst et al., 2001; Koulakov and Chklovskii, 2001). The primary visual cortex of carnivores and primates contains multiple, superimposed functional maps that represent the visuotopic location, orientation, spatial frequency, movement direction, and ocular dominance of visual stimuli (Hubel and Wiesel, 1963; Blasdel and Salama, 1986; Shmuel and Grinvald, 1996; Hübener et al., 1997).

Anatomically, intrinsic lateral connections show a repeating patchy structure when viewed in a plane parallel to the cortical surface (Rockland and Lund, 1982) whose interpatch distance is similar to the spatial wavelength of functional maps. Functional-anatomical studies using

Grant sponsor: Deutsche Forschungsgemeinschaft; Grant number: SFB509, TPA6 (to Z.F.K.).

*Correspondence to: Péter Buzás, Institute of Physiology, Medical School, University of Pécs, Szigeti út 12, Pécs 7643, Hungary. E-mail: peter.buzas@aok.pte.hu

Received 4 January 2006; Revised 12 May 2006; Accepted 29 June 2006

DOI 10.1002/cne.21134

Published online in Wiley InterScience (www.interscience.wiley.com).

metabolic (Gilbert and Wiesel, 1989; Löwel and Singer, 1992), electrophysiological (Kisvárdy et al., 1997), or optical mapping (Malach et al., 1993; Kisvárdy et al., 1994; Bosking et al., 1997) in combination with neuron tracing have examined the possible rules accounting for this relationship. These studies suggest that the strength of connections depends on functional similarity between cortical sites. In line with this, nearby neurons that represent the same visuotopic location and share most of their receptive field (RF) properties show the strongest correlation in their firing (Ts'o et al., 1986; Hata et al., 1991).

Computer simulations of the visual cortex often explicitly incorporate the distribution of lateral connections in the form of cortical interaction functions. In such artificial networks, connection probability is defined to change with distance from the source neuron, where "distance" can be along the spatial (McLaughlin et al., 2000) and/or a functional dimension, such as orientation preference (Somers et al., 1995; Koulakov and Chklovskii, 2001). In the simplest and most widely used form, connection probability follows isotropic Gaussian or related functions (McLaughlin et al., 2000; Koulakov and Chklovskii, 2001), although there has been considerable effort to study other types of lateral connection patterns (Adorján et al., 1999; Shouval et al., 2000; Ben-Shahar and Zucker, 2004; Carreira-Perpiñán and Goodhill, 2004; Yu et al., 2005). However, these theoretical connection functions have rarely been validated on the basis of anatomical data.

Most experimental studies to date have examined intracortical connections using extracellular injection of retrograde or anterograde neuronal tracers (Gilbert and Wiesel, 1989; Malach et al., 1993; Bosking et al., 1997; Kisvárdy et al., 1997). This technique shows the compound pattern of tens to hundreds of labeled neurons, which we here refer to as "population level" connectivity. But connectivity rules identified at the population level might not apply equally to the members of the population. Indeed, the signaling characteristics of even close-by cortical neurons can be unique, with individual deviations from the average (Albus, 1975; DeAngelis et al., 1999; Hetherington and Swindale, 1999; Reich et al., 2001). However, the extent of individual differences with respect to their functional connectivity is not known.

The aim of this study is to compare the spatial and orientation distribution of excitatory boutons found at the population and the single-cell level. To this end, we combined optical imaging of intrinsic signals and anatomical tracing in order to explore the relationship between the orientation map and intrinsic excitatory lateral connections in the cat primary visual cortex. First, we demonstrate that the radial and orientation distribution of connections formed by large populations of neurons can be adequately explained by a model assuming similarity of spatial location and orientation as described by simple tuning functions. Then we examine the ability of this model to predict single-cell connection patterns. We find that single-cell axonal connections often cannot be fully explained by the population model and their estimated spatial and orientation tuning functions are highly variable. We conclude that the spatial and orientation-specific intrinsic excitatory network is composed of neurons following various connectivity rules.

MATERIALS AND METHODS

Nine adult cats (8–14 months old) underwent combined optical imaging of intrinsic signals and anatomical labeling experiments. All surgical procedures were in accordance with the German Animal Welfare Act and conformed with the European Communities Council Directive of November 24, 1986 (86/609/EEC).

Surgical preparation

The animals were prepared for surgery using procedures described previously (Buzás et al., 1998; Yousef et al., 1999). Briefly, anesthesia was induced with a mixture of ketamine (7 mg/kg, Ketanest, Parke-Davis, Berlin, Germany) and xylazine (1 mg/kg, Rompun, Bayer Belgium, Sint-Truiden, Belgium) intramuscularly (i.m.). The eyes were protected against dehydration using hyperosmotic eye drops (1.5% saline) and neutral contact lenses. The nictitating membranes were retracted and the pupils dilated with 5% phenylephrinhydrochlorid (Neosynephrin-POS, Ursapharm, Saarbrücken, Germany) and 1% atropine sulfate (Atropin-POS, Ursapharm, Saarbrücken, Germany), respectively. The femoral artery was cannulated and a tracheal cannula implanted. Anesthesia was maintained throughout the experiment using 0.4–0.6% of halothane (Halothan Eurim, Eurim-Pharm, Piding, Germany) and artificial ventilation with a 1:2 mixture of O₂ and N₂O. For muscle relaxation, alcuronium chloride (0.15 mg/kg/h, Alloferin, Hoffman-La Roche, Grenzach-Whylen, Germany) was infused with glucose (24 mg/kg/h) and Ringer solution (Ringerlösung Fresenius, Fresenius, Bad-Homburg, Germany) via the femoral catheter. End-tidal CO₂ (3–4%), blood pressure (100–140 mmHg peak), and body temperature (38°C) were monitored and kept in normal ranges. In intracellular labeling experiments, a bilateral pneumothorax was prepared to reduce brain movement related to artificial ventilation.

Craniotomies were made in both hemispheres between Horsley-Clarke coordinates AP (-)4 and (+)9 and LM (+)0.5 and (+)6.5 to give access to the representation of the lower-central visual field (up to about 15° eccentricity) in area 18, the 17/18 border, and area 17 (Tusa et al., 1978, 1979). A metal chamber was mounted over the exposed region using dental cement (Paladur, Heraeus Kulzer, Wehrheim, Germany). After the dura mater had been removed, the chamber was filled with silicone oil (Aldrich, Milwaukee, WI) and sealed with a round coverglass.

Optical imaging of intrinsic signals

Optical imaging of intrinsic signals was carried out using the imaging system Imager 2001 (Optical Imaging, Germantown, NY) according to procedures described earlier (Bonhoeffer and Grinvald, 1996; Buzás et al., 1998). Briefly, the cortex was illuminated with a circular fiber optic slit lamp (Schott, Mainz, Germany) surrounding the camera optics (two SMC Pentax lenses, 1:1.2, $f = 50$ mm, arranged in a "tandem" manner; Ratzlaff and Grinvald, 1991). For imaging the vascular pattern of the cortical surface, 545 ± 10 nm (green) light was used. These high-contrast images were used together with reference penetrations (see below) for aligning the optical images with the anatomical data. During data acquisition of intrinsic signals the camera was focused 650–750 μm below the cortical surface and the cortex was illuminated with 609 ± 5 nm light. The refraction of the eyes was corrected for the

stimulus viewing distance by contact lenses on the basis of tapetal reflection. Visual stimuli were full-field, high-contrast, achromatic square-wave gratings (0.1–0.3 cycle/deg spatial and 1–2 Hz temporal frequencies), generated using the stimulus generation systems Vision Works (Vision Research Graphics, Durham, NH) or VSG Series Three (Cambridge Research Systems, Rochester, UK) and presented binocularly on a video screen (Sony, Pencoed, UK) in 120-Hz noninterlaced mode. The stimuli subtended a 40–60° visual angle, sufficient to cover the animals' visual field represented in the imaged cortical region in both eyes, taking into account the divergence of the eyes due to muscle relaxation. For obtaining orientation preference maps, a single stimulus trial consisted of eight gratings of four equally spaced orientations (0°, 45°, 90°, 135°), each drifting in one direction with optimal velocity along the orthogonal axis displayed in a pseudorandom sequence. Each image acquisition period was preceded by an interstimulus interval of 10 seconds when the animals viewed a stationary image of the next grating stimulus. Video frames were acquired for 4.5 seconds, commencing 1 second after the stimulus grating began to move. Two by two image pixels were binned together to obtain the final data frames.

Single condition maps (SCMs) were calculated by summing the images associated with each orientation using the MIX software (Optical Imaging). All SCMs were normalized to the cocktail blank (Bonhoeffer and Grinvald, 1993), i.e., the sum of images recorded for all stimulus conditions. The SCMs were rescaled to the range between 0–255 while clamping extreme values (outside the range of $\pm 1.5\text{--}3$ times the mean absolute deviation around the mean) to 0 or 255. Saturation of pixel values (0 or 255) was allowed only in regions containing reflection artifacts outside the exposed cortical tissue. Subsequent calculations were performed using a custom-made program written in the IDL language (Research Systems, Boulder, CO). The SCMs were bandpass-filtered using averaging kernels of 1064 μm (50 pixels, high-pass) and 106–404 μm (5–19 pixels, low-pass). Orientation angle maps were computed using pixel-by-pixel vectorial summation of orientation SCMs (Blasdel and Salama, 1986; Bonhoeffer and Grinvald, 1991). Masks were created for each orientation map to exclude pixels where the map could not be determined due to bone, major blood vessels, or the convolutions of the cortex.

At the end of the optical imaging experiment, about 1 mm-deep reference penetrations were made in the cortex using an empty micropipette driven parallel with the optical axis of the imaging camera. The entry points were registered on the image of the cortical surface. The reference penetrations were used later to align the optical images with the histologically reconstructed structures.

Tracer injections

Extracellular iontophoretic injections of biocytin (2% solution; Sigma, Deisenhofen, Germany), biotinylated dextran-amine (BDA, 2% solution, Molecular Probes, Leiden, Holland), or horseradish peroxidase (HRP, 4% solution, Sigma) were made into layers 3 to 5 of the imaged cortex regions using borosilicate glass micropipettes (GB10F-10, Science Products, Hofheim, Germany; inner diameter 0.58 mm, tip size 6–8 μm). In the population labeling cases (two animals), only one injection per hemisphere was made into the superficial layers at 0.3–0.4 mm

below the cortical surface. Where the aim was to retrogradely label single neurons (five animals), injections were made at multiple locations. The entry points of the injection pipettes were marked on the surface image of the imaged region. The tracers were delivered iontophoretically using positive 0.6–1 μA current pulses (0.5–1 Hz square-wave, 50% duty cycle) for 15–22 minutes.

Intracellular injections (two animals) were made as described by Buzás et al. (1998). Briefly, sharp borosilicate glass micropipettes pulled on a horizontal puller (Sutter Instrument, Novato, CA) were filled with freshly prepared 0.5 M K-acetate containing 1–2% biocytin and beveled on a BV-10 micropipette beveler (Sutter Instrument), decreasing their input resistance from an initial 100–120 $\text{M}\Omega$ to 40–105 $\text{M}\Omega$. A micropipette was positioned into its desired location and advanced to penetrate the pia mater. The open recording chamber was filled with a thick layer of low melting point (42–44°C) paraffin wax (Merck, Darmstadt, Germany). The micropipette was advanced until a sudden 40–70 mV drop in the membrane potential was registered, indicating successful penetration of a neuron's cell membrane. After determining visual responsiveness and approximate RF position of the cell using handheld stimuli, biocytin was injected iontophoretically into the cell using positive 2–3.5 nA rectangular current pulses (1.7 Hz, 33% duty cycle) for 1–5 minutes.

Histological procedures

After tracer injections (1–24 hours), the animals were killed using a lethal dose of anesthetics (5% halothane) and were perfused transcardially with Tyrode's solution followed by a mixture of 2% paraformaldehyde and 0.1–0.2% glutaraldehyde in 0.1 M phosphate buffer (PB; pH 7.6). Tissue blocks containing the optically imaged regions were dissected and 30–40 consecutive, 60–70- μm thick sections were cut on a vibratome, with the cutting plane set as parallel to the imaged cortical surface as possible. We have found that this thickness is a good compromise between preservation of the tissue and reagent penetration (e.g., Buzás et al., 2001). The free-floating sections were rinsed in 0.1 M PB for 3 \times 20 minutes and the biocytin and BDA labeling was visualized using the avidin-biotin complexed HRP (ABC, Vector Laboratories, Burlingame, CA) method (Horikawa and Armstrong, 1988). The HRP enzymatic reaction was revealed with 0.005% 3,3'-diaminobenzidine-4-HCl (DAB; Sigma) supplemented with 0.0025% CoCl_2 (Adams, 1981) in Tris-buffered saline (pH 7.6) for 20 minutes and completed in the presence of 0.001% H_2O_2 for 1–3 minutes. The sections were postfixed in 0.5–1% OsO_4 in 0.1 M PB for 10–20 minutes and dehydrated in ascending series of ethanol. Finally, the sections were transferred into propyleneoxide for 2 \times 15 minutes and embedded in Durcupan ACM (Fluka, Neu-Ulm, Germany) on microscopic slides (Somogyi and Freund, 1989).

The photographs were taken with 50 \times and 100 \times objectives using a Leica DMRB light microscope (Wetzlar, Germany) and a Canon EOS D60 (Tokyo, Japan) digital camera. The images were stored on a PC, converted to grayscale at 600 dpi, and enhanced in contrast using manual adjustment in the Corel Photo-Paint 9 image processing software (Corel, ON, Canada).

TABLE 1. Main Data of the Anatomical Reconstructions

Case	Population 1	Population 2	PY3.1	PY3.2	PY3.3	PY3.4	PY4.1	PY4.2	SS4.1	PY5.1	PY5.2	Single cells pooled
Tracer	Biocytin	Biocytin	Biocytin	BDA	BDA	BDA	Biocytin	Biocytin	HRP	Biocytin	Biocytin	
Injection method	Extracell.	Extracell.	Intracell.	Extracell.	Pyramidal	Pyramidal	Extracell.	Extracell.	Extracell.	Extracell.	Extracell.	
Morphological class	Excitatory	Excitatory					Pyramidal	Pyramidal	Spiny stellate	Pyramidal	Pyramidal	Excitatory
Somata												
Laminar position	1–6	1–6	3	3	3	3	4	4	4	5	5	3–5
Dendritic tree												
Maximum radial extent (μm)			435	230	193	194	240	238	178	491	195	491
Axon tree												
Maximum radial extent (μm)	2,475 ¹	2,897 ¹	2,184	1,480	1,353	856	2,850	1,810	1,702	2,930	2,003	2,930
Boutons												
Total number	299,730	130,728	3,949	1,046	1,295	1,844	1,232	1,430	1,348	1,879	6,184	20,207
Layers 1–4	242,883	120,205	3,321	1,046	1,124	1,813	1,133	1,211	1,014	1,790	6,123	18,575
In regions with valid orientation map (% of layers 1–4)	99.6	82.4	100.0	97.8	100.0	100.0	90.2	100.0	100.0	100.0	100.0	99.3

The names of the single cells refer to their morphological type and laminar position of their somata. BDA: biotinylated dextrane-amine, HRP: horseradish peroxidase.

¹Within valid region of orientation map.

Three-dimensional reconstructions

Labeled axonal connections were reconstructed at 1,000 \times magnification using a light microscope (Leica DMRB) fitted with a drawing tube alone or the neuron reconstruction system, Neurolucida (MicroBrightField, Colchester, VT). In order to reconstruct population labeling, tissue blocks containing a single extracellular tracer injection per hemisphere were used. The position of all labeled axonal boutons was digitized in two dimensions (2D) from consecutive sections throughout all cortical layers. The series of 2D reconstructions was then merged into a three-dimensional (3D) dataset by assigning to each section a depth value in increments of section thickness. In a separate but aligned reconstruction, only inhibitory type boutons were taken into account, which were distinguished from excitatory type boutons on the basis of morphological criteria (Kisvárday et al., 1997). The distribution of excitatory connections was then calculated by subtracting the inhibitory bouton density maps from the map of the total boutons. In order to reconstruct single spiny neurons, strongly labeled cells were selected whose dendritic spines and axonal boutons were clearly visible. Their labeled somata, dendritic, and axonal processes and boutons were digitized in 3D from adjoining sections (Table 1). We aligned the neighboring sections with the help of corresponding cut ends of labeled neuronal processes or small blood vessels in the estimated projection field of the reconstructed connections. For single cells, we marked each bouton according to its cortical layer. The borders of cortical layers were determined in tangential sections on the basis of light microscopic characteristics visible in the osmium-treated tissue, such as relative neuron and fiber densities, neuronal soma size, and the presence of large pyramidal cells at the border region of layers 3 and 4 and giant pyramidal cells of Meynert in layer 5b.

Alignment of the reconstructions with the functional maps

The 3D digitized anatomical data were transformed into the coordinate system of the optical maps as described earlier (Kisvárday et al., 1994; Buzás et al., 1998). Here, common reference points in the histological reconstruc-

tions and the optical images (the locations of the reference penetration and tracer injection tracks, surface blood vessels) were aligned using linear transformations (rotation, translation, and scaling).

We use the term “site of origin” of the connections to denote the point where the labeled axons originated. For the population cases, the site of origin corresponded to the injection site. For single cells, the point was taken where an imaginary line, which passed through the cell body and ran orthogonal to the cortical surface, crossed layer 2/3. This point was then projected to the imaging plane.

Bouton density maps and distributions

Bouton density maps were created by projecting the boutons onto the plane of optical maps and binning them at the same pixel resolution. In this process, only the upper layer boutons were included even if the parent cell bodies were in the deeper layers. For single cells, boutons in layers 1–4 were included. In the case of the population labeling, boutons between the pia and 750 μm (for Population 1) or 774 μm (for Population 2) in depth were selected, encompassing layers 1 to upper 4.

Each labeled bouton and cell body was characterized by the orientation angle value of the corresponding pixel. We refer to the “orientation preference of a bouton” for the sake of simplicity, although boutons have no orientation preference in the same sense as neurons do.

Where bouton density is expressed as a function of three variables, i.e., the spatial coordinates x and y and orientation preference φ , we call this a *trivariate distribution*. The distribution of boutons was also expressed as function of two variables: radial distance from the site of origin and orientation, which we refer to as the *bivariate distribution* (see 2D histograms in Figs. 8, 9). The latter was obtained by rebinning the trivariate distribution, using the following parameters: bin width for radial distances: 100 μm; orientation bin width: 10°; the range of radial distances was 0–3,000 μm from the site of origin. *Univariate distributions* (line plots in Figs. 8, 9) were calculated to express the number of boutons separately as a function of lateral distance or orientation.

TABLE 2. Model-Fitting Results

Case	Population 1	Population 2	PY3.1	PY3.2	PY3.3	PY3.4	PY4.1	PY4.2	SS4.1	PY5.1	PY5.2	Single cells pooled
Absolute orientation preference of site of origin (deg)	163.7	6.6	23.5	104.4	123.2	73.5	72.5	68.0	74.3	117.6	147.6	n.a.
Independent estimates of the univariate distributions												
Spatial dispersion, σ_0 (μm)	623.6	580.3	520.8	493.7	350.6	217.7	552.6	512.7	344.4	944.9	918.1	694.1
Mean orientation angle, μ_0 (deg)	6.7	-3.70	5.6	-12.7	-0.8	-4.1	-3.1	-2.2	-16.5	2.6	-26.6	-8.2
Orientation selectivity, κ_0	0.98	1.07	1.04	0.98	1.90	0.95	1.19	0.93	2.08	1.07	0.72	0.87
HWHH of orientation tuning (deg)	36.5	34.7	35.3	36.5	25.3	37.2	32.7	37.6	24.1	34.7	43.9	39.0
Full model parameter estimates												
R^2_{2D}	0.87	0.95	0.68	0.41	0.84	0.90	0.53	0.80	0.86	0.42	0.31	0.83
Oriented component												
Spatial extent, σ_{21} (μm)	1,105	889	731.4	808.5	214.8	162.2	444.1	1,171	118.1	1,460	1,918	1,088
Orientation selectivity, κ_2	1.20	0.67	0.63	1.21	17.94	2.37	6.66	0.61	3.81	1.11	1.32	0.58
Orientation preference, μ_2 (deg)	7.2	-7.1	9.2	-21.0	2.1	-20.2	2.6	-2.6	-22.5	16.8	-17.6	-12.6
Scaling factor, m	10.6	14.6	17.4	49.2	3.9	2.2	5.9	6.6	4.1	19.8	13.4	18.0
Nonoriented component												
Spatial extent, σ_{22} (μm)	260.4	273.6	145.6	114.7	520.2	221.7	878.2	138.5	490	172.5	1,359	144.1
Oriented component ratio (M)	58%	65%	72%	87%	61%	36%	51%	39%	56%	71%	60%	69%

HWHH, half-width at half-height of the von Mises function with parameter κ_0 .

Target soma density estimate (TSDE) maps

The majority of excitatory connections are formed with dendritic processes (Kisvárdy et al., 1986; Gabbott et al., 1987; McGuire et al., 1991); therefore, a bouton will generally be at some distance from the target cell body. We estimated the density of target somata by convolving bouton distribution maps with a kernel describing the probability density of postsynaptic somata around a bouton. The profile of the kernel was based on Sholl-type (Sholl, 1955) dendritic density data obtained from 28 reconstructed pyramidal neuron dendritic trees. Here the 3D reconstruction of each dendritic tree was projected onto the plane orthogonal to the apical dendrite. Dendritic density was measured as the number of points of the digitized dendrite in $\sim 20\text{-}\mu\text{m}$ bins of radial distance from the soma. Dendritic density was normalized for between-cells comparison and averaged over all cells (Fig. 11A, filled circles). A good fit to these data was obtained using a univariate Gaussian distribution with a mean = 100 μm and standard deviation (SD) = 50 μm (Fig. 11A, open squares). Revolving this profile around the ordinate and normalizing the resulting integral volume created an annular convolution kernel (Fig. 11A, inset). The convolved density maps are referred to as target soma density estimate (TSDE) maps. We performed this analysis for the first population case and the single-cell cases ($n = 10$).

Independent estimates of the univariate distributions

One way of modeling the univariate distributions was to treat cortical distance and orientation preference as independent variables (Fig. 7). After normalizing the total number of boutons to 1, the radial distribution was assumed to follow the Rayleigh probability density function:

$$F(r, b) = \frac{r}{b^2} e^{-\frac{r^2}{2b^2}}, \quad (1)$$

where r is the lateral cortical distance from the site of origin and b is the Rayleigh parameter. This distribution is obtained from an isotropic 2D Gaussian distribution by expressing its integral along concentric circles as a function of the radius. Parameter b of the Rayleigh distribu-

tion equals the σ of this Gaussian. The maximum likelihood estimate of this value is called here “spatial dispersion” and calculated as:

$$\sigma_0 = \sqrt{\frac{1}{2N} \sum_i n_i r_i^2}, \quad (2)$$

where i scans through all valid pixels of the orientation map, n_i represents the number of boutons in the i -th pixel, r_i is its distance from the site of origin, and N is the total number of boutons (Statistics Toolbox User’s Guide, MathWorks, Natick, MA).

The orientation distribution of boutons was assumed to follow the von Mises distribution defined for angles of orientation as:

$$V(\varphi, \kappa, \mu) = \frac{1}{2\pi I_0(\kappa)} e^{\kappa \cos 2(\varphi - \mu)}, \quad 0 \leq \mu < \pi \quad (3)$$

where φ is the orientation preference of the map pixel relative to the site of origin, μ is the orientation at the center of the distribution, κ is the concentration parameter, and $I_0(\kappa)$ is the modified Bessel function of the first kind of zero order (Batschelet, 1981; Swindale, 1998). The maximum likelihood estimate of μ (mean relative orientation, μ_0) is the mean angle obtained by vectorial summation of each bouton’s relative orientation preference. The estimate of the κ parameter (κ_0) was determined from the length of the vector sum of orientations using the corresponding table by Batschelet (1981). We used κ_0 to express the orientation selectivity of the bouton distribution (the higher its value the narrower the orientation distribution). For a comparison with other studies, we also calculated the half-width at half-height (HWHH) of the von Mises function (Table 2) using equation 6a of Swindale (1998).

Modeling the surface-view distribution of boutons

To define a quantitative model, we assumed that bouton density maps are determined by the orientation difference and spatial position of the target sites relative to the site

of origin (see above). The dependence of bouton density on these factors was expected to follow simple distribution functions, to which we refer here as orientation and spatial tuning of the connections. Since this model involves three independent variables (the 2D cortical coordinates and orientation preference), we call it the *trivariate model*. To model the spatial tuning of connections, we used a 2D, isotropic Gaussian function (G) that was centered on the injection site:

$$G(x, y, \sigma) = \frac{1}{2\pi\sigma^2} e^{-\frac{x^2+y^2}{2\sigma^2}}, \quad (4)$$

where x and y are the cortical coordinates and σ is the SD of the Gaussian. The orientation tuning of connections was modeled by the von Mises function as defined in Eq. 3.

In the simpler *one-component* version of the model, the number of boutons was considered proportional to the product of the two tuning functions. Thus, the model was defined as:

$$D_1(x, y, \varphi) = s_1[G_{11}(x, y, \sigma_{11})V_1(\varphi, \kappa_1, \mu_1)], \quad (5)$$

where functions V_1 and G_{11} are as in Eqs. 3 and 4, with corresponding parameters. The scaling parameter s_1 represents the total number of boutons divided by the sum of the model (before scaling), so that the sum of the scaled model is the same as the total bouton number.

In the *full* or *two-component* model, an oriented and a nonoriented component were summed. The former corresponded to the one-component model of Eq. 5, whereas the latter was an isotropic Gaussian term:

$$D_2(x, y, \varphi) = s_2[mG_{21}(x, y, \sigma_{21})V_2(\varphi, \kappa_2, \mu_2) + G_{22}(x, y, \sigma_{22})], \quad (6)$$

where functions V_2 , G_{21} , and G_{22} are as in Eqs. 3 and 4, with corresponding parameters and m sets the weight of the oriented component. The mixing ratio of the oriented and nonoriented components (Table 2) can be calculated after the model fitting as:

$$M = \frac{\sum_{map} mG_{21}V_2}{\sum_{map} (mG_{21}V_2 + G_{22})}, \quad (7)$$

where *map* includes all valid pixels of the orientation map (function arguments are omitted for clarity). Plots of the two components and the full model are shown in Figure 5D–F.

Model fitting

Model fitting was performed on the bivariate distributions (2D histograms in Figs. 8, 9) created from the trivariate model by rebinning (see “Bouton density maps” above). This technique had multiple advantages compared to attempting to describe the bivariate distribution directly. First, it allowed us to build the model equation from the simple Gaussian and von Mises tuning functions. Second, we could take into account the nonuniform sampling of the independent variables due to masked-out re-

gions of the cortical surface and the possible nonuniform representation of different orientations in the map. The modeled bivariate distribution was fit to the experimental data in such a way that the free parameters of the trivariate model (σ_{11} , μ_1 , κ_1 for the one-component model, σ_{21} , μ_2 , κ_2 , σ_{22} , and m for the full model) were adjusted and the sum of squared errors between the experimental and modeled bivariate distributions was minimized. Minimization was performed using the “constr” function in the Matlab Optimization Toolbox (MathWorks) imposing the following constraints on parameters: $0 < \sigma$, $-90^\circ \leq \mu \leq 90^\circ$, $0 < \kappa$, $0 < m$. For simplicity, the best fit parameter estimates were labeled by the same letters as the model parameters. Figure 5D–F illustrates the trivariate model and its components that gave rise to the best-fit bivariate distribution for Population 1 (Fig. 8A, right-hand side).

The goodness of fit of the model is given by the R^2 statistics, which express the fraction of variance explained by the model. R^2_{2D} denotes the goodness of fit of the bivariate model, whereas R^2_{ori} and R^2_{rad} compare the data and model with respect to their univariate distributions as a function of orientation and radial distance, respectively.

RESULTS

We examined the relationship between excitatory lateral connections and orientation maps in the cat primary visual cortex using a combination of intrinsic signal optical imaging and anatomical labeling of large populations of neurons or single cells. Connectivity was inferred from the presence of axonal boutons, which are the light-microscopic correlates of the axons’ output synapses (Kisvárdy et al., 1986; Gabbott et al., 1987; Anderson et al., 1994).

Morphology of excitatory lateral connections

Figure 1A shows the biocytin labeling after an extracellular injection into layer 3 of area 18 with a core diameter of about 150 μm . This is one of the two injections used to label the axons originating from populations of nearby excitatory neurons (case Population 1). Typically, the labeled somata ($n = 187$) were concentrated around the injection site, although a few retrogradely labeled cells were found up to 1,450 μm from the injection center. Labeled neurons in the vicinity of the injection site seemed to provide the majority of labeled axons and boutons, whereas those more remote were unlikely to contribute significantly to the total bouton population because their axons were most often not or only faintly labeled. Within the optically imaged regions and the analyzed range of depth (see Materials and Methods), the bouton labeling extended up to 3 mm laterally from the injection site.

The most important morphological data of the reconstructed structures are summarized in Table 1. For the analysis of single cells, nine spiny neurons (one spiny stellate and eight pyramidal) were reconstructed following either extracellular ($n = 7$) or intracellular ($n = 2$) injections (see Table 1 for details). High-power micrographs demonstrate the typical morphology of pyramidal cells (Fig. 1B) and their axons (Fig. 1C) labeled retrogradely from extracellular injections. Reconstructions of three representative cells, with somata in layers 3, 4, or 5, are

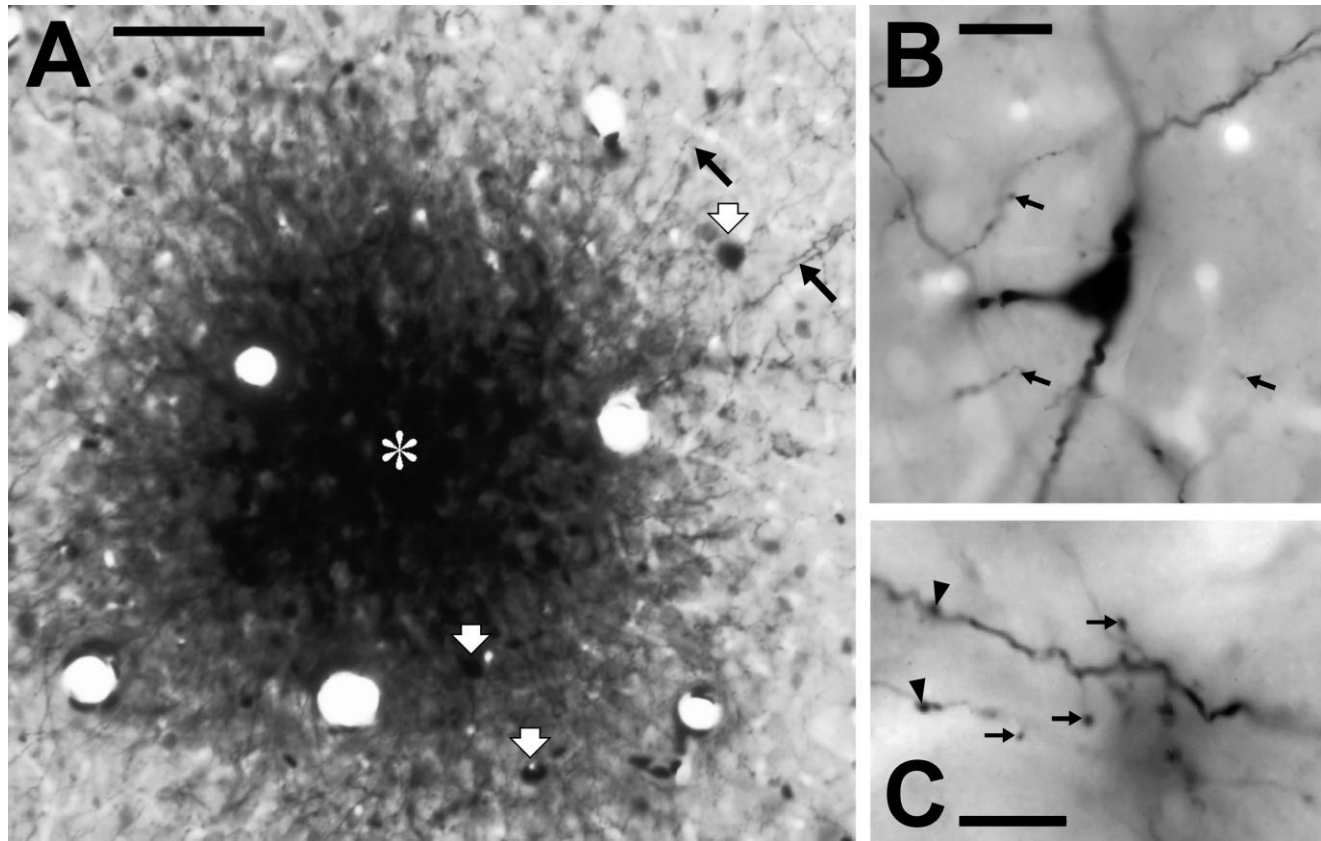


Fig. 1. Extracellular biocytin labeling of horizontal connections in area 18. **A:** Tangential section through the core of the injection site of case Population 1 (asterisk) at the level of layer 3. Labeled somata (thick white arrows) and radiating axon bundles (black arrows) are marked in the vicinity of the darkly stained injection site. **B:** Photomontage of a retrogradely labeled pyramidal cell that was found 650

μm laterally from the injection site shown in A. Arrows mark nearby axon collaterals of the same pyramidal cell. **C:** High-magnification image taken from one of the axon clusters labeled from the injection site in A. Both thin and thick axons possess en passant (arrowheads) and club-like (arrows) boutons emitted most likely by pyramidal neurons. Scale bars = 100 μm in A; 20 μm in B; 10 μm in C.

shown in detail in Figures 2–4. We limited our quantitative analysis to layers 1–4 because these are known to contain most long-range lateral connections (in layer 2/3) as well as the main feed-forward projection from layer 4 to layer 2/3 (Anderson et al., 1994; Binzegger et al., 2004; Yoshimura et al., 2005). In our sample, layers 1–4 contained the majority of boutons (75–100%, Table 1, black dots in Figs. 2–4) for each cell, regardless of the laminar position of the soma, and they included the longest lateral connections. Figure 6 shows for all single cells used in the analysis the superimposition of these terminals (black dots) onto the corresponding orientation maps.

Bouton density maps of the two population cases are shown in Figure 5A,G. Similar to earlier descriptions (Rockland and Lund, 1982; Gilbert and Wiesel, 1989; Löwel and Singer, 1992; Malach et al., 1993; Kisvárdy et al., 1994, 1997; Bosking et al., 1997), these maps revealed dense, isotropic local regions of label in the vicinity of the injection sites, surrounded by patches of long-range connections. The patches formed a repeating pattern, with their centers on average $1,282 \pm 384$ μm from the site of origin. Note, however, that no distinct border could be drawn between these local and long-range types of connections; rather, they appear to be superimposed on each other.

The density maps of boutons originating from individual cells (Fig. 6) revealed large variability between cases. First, the contribution of local boutons varied considerably from cell to cell. For example, the spiny stellate cell (Fig. 3) and some pyramidal cells (Fig. 6C,D) had dense plexuses around the soma, whereas other pyramidal neurons (Figs. 4, 6B,I) almost lacked local connections. Second, long-range connections were often not clearly organized in patches (Fig. 6B,C,E) and included long series of en passant boutons or the size, density, and shape of patches varied (Figs. 2, 4, 6A,E–I). We also noted that the center of gravity of the local connections was usually shifted from the location of the parent soma (Figs. 2–4, 6) as opposed to the isotropic core region typically found in the population cases (Fig. 5A,G). As will become evident below, these morphological features strongly impact on the observed relationship of lateral connections to the underlying orientation map.

Radial and orientation distribution of lateral connections

The distribution of lateral connections can be theoretically related to any functional property represented in the cortex, or even entirely lack such correlation. In this sec-

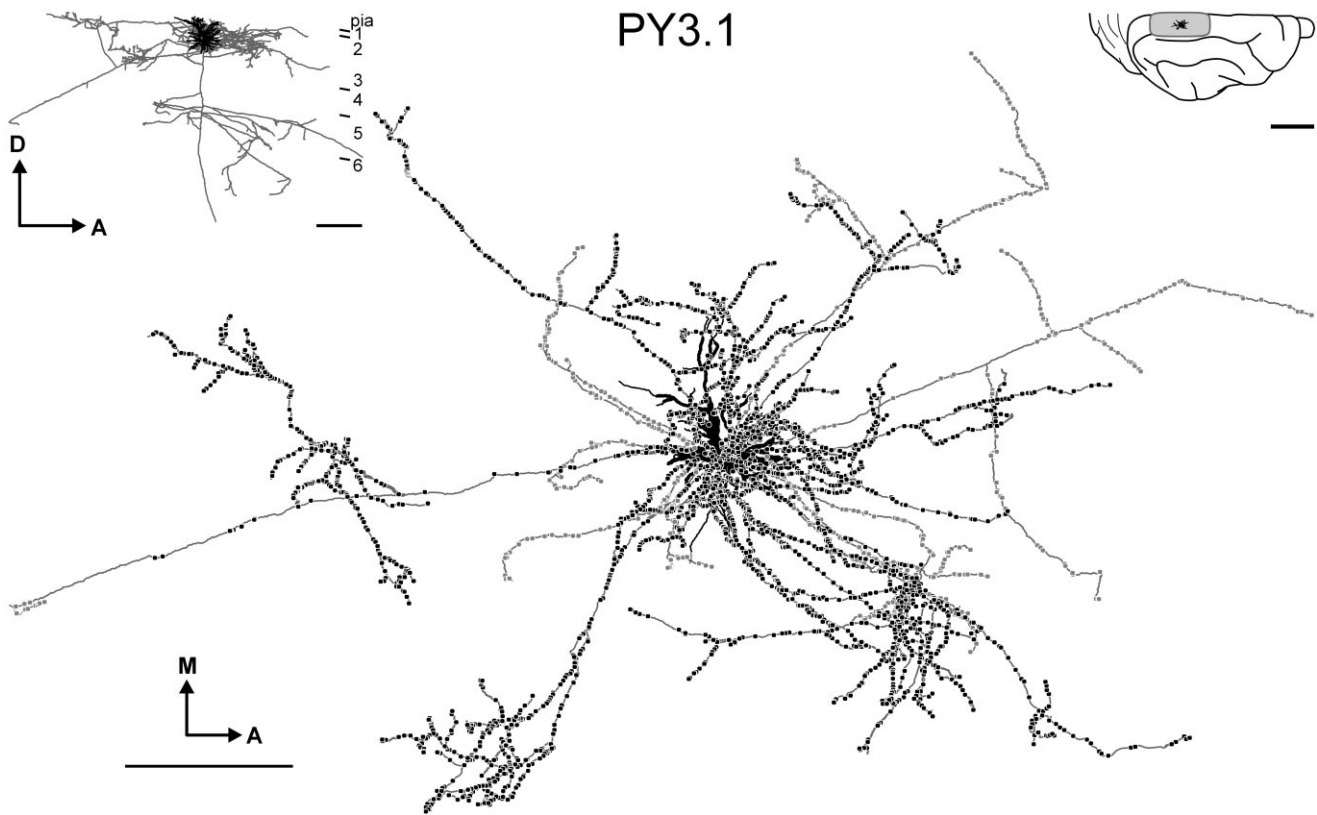


Fig. 2. Anatomical reconstruction of an intracellularly filled layer 2/3 pyramidal cell (cell PY3.1). The main panel shows the 3D reconstruction viewed so that the plane of the paper corresponds to that of the optical images of the surrounding region. The axon tree (gray) forms extensive lateral connections in the supragranular as well as infragranular layers. Dense local connections are part of an elongated, slab-like region of terminals extending postero-medial to antero-lateral across the soma. Some axon segments are completely void of boutons while traveling to remote patches. Axonal boutons in the different

layers are shown by dots along the axon (black dots: layers 1–4, gray dots: layers 5–6). The dendritic tree (black) is drawn behind the axon to avoid clutter. The top-right inset shows the dorsal view of the right hemisphere and indicates the relative size of the axonal field of the cell (black) within the approximate region exposed for optical imaging (gray shading). The top-left inset shows the cell reconstruction viewed in the parasagittal plane with the pia mater and cortical layers indicated. A, anterior; M, medial; D, dorsal. Scale bars = 500 μ m in reconstructions, 10 mm in cat brain inset.

tion we explore the possibility that selectivity to cortical location or to orientation preference alone can account for the observed distributions.

Radial distribution. The patchy pattern of the population distribution described above was accompanied by a gradual decline of bouton density with radial distance from the injection site (Fig. 5A,G). The overall decrease in bouton density was consistent with a Gaussian-shaped envelope centered on the site of origin, as can be illustrated by plotting the number of boutons against radial distance (Fig. 7A). In this view, an isotropic 2D Gaussian in the cortical plane appears as a Rayleigh distribution (Eq. 1). The b parameter of the Rayleigh distribution is equivalent to the SD (σ) of the corresponding 2D Gaussian (Eq. 4), which we estimated from each dataset (σ_0 , Eq. 2) and used as a measure of the spatial dispersion of the boutons. Its value was 624 and 580 μ m in the respective population cases (Fig. 7A, Table 2). The obvious difference between the simple Gaussian model (dashed lines) and the data (solid lines) can be attributed to the clustering of boutons. The peaks close to the origin (~250–300 μ m) were mainly due to the isotropic core of the labeling, whereas the remote patches (Fig. 5A,G) caused peaks at

regular distances between 1,200 and 2,100 μ m. The single-cell data show the same general features as the population cases (Fig. 7E), except for a large individual variability in spatial dispersion (σ_0 ranging from 218–945 μ m, Fig. 7G) in the number of peaks and in their relative heights. Nevertheless, their σ_0 values were scattered around those of the populations showing no statistically significant differences ($P = 0.70$, Student's t -test).

Orientation distribution. Figure 5 shows the aligned bouton density (Fig. 5A,G) and orientation (Fig. 5B,H) maps for the population cases. Confirming results of earlier studies (Malach et al., 1993; Kisvárday et al., 1994, 1997; Bosking et al., 1997), the isotropic centers of label covered all orientations within their spatial extent, whereas the more remote patches (marked by crosses in Fig. 5) overlapped with regions of similar orientation preference to the center (circle markers in Fig. 5B,C,H). The axon terminals of the single cells often concentrated in orientation domains similar to the soma location (Fig. 6A,E,F,H,I), but in general each cell contacted a wide range of orientations.

For a quantitative analysis, the orientation preference of each injection site and individually reconstructed cell

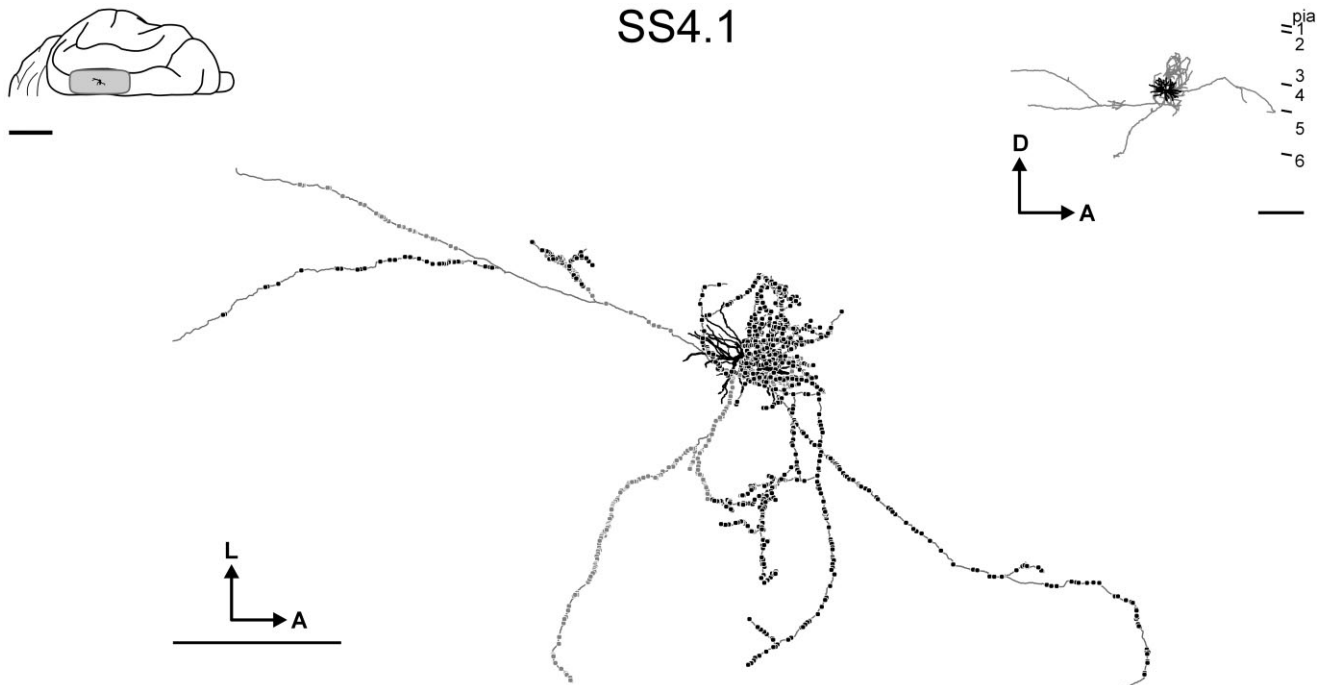


Fig. 3. Anatomical reconstruction of an extracellularly filled spiny stellate cell (cell SS4.1). The conventions are the same as in Figure 2. The axon tree (gray) formed dense connections in the vicinity of the soma with its center of gravity shifted to anterolateral. Most of the collaterals leaving this region were sparsely branched except for some

concentration of terminals medially from the soma. The spinous dendrites formed a dendritic tree (black) of typical stellate morphology. A, anterior; L, lateral; D, dorsal. Scale bars = 500 μ m in reconstructions, 10 mm in cat brain inset.

body was determined from the optically imaged maps and these values are reported in Table 2. Hereafter, the orientation preference of each bouton's location was measured relative to the respective site of origin. The orientation preference distribution of the population connections followed a unimodal bell shape (Fig. 7B), whereas single-cell distributions showed secondary peaks or were skewed (Fig. 7F). Figure 7B,H,I shows the approximation of these curves with the von Mises distribution (Eq. 3), which has been suggested (Swindale, 1998) to be the optimal model of cortical neuron orientation tuning. The two parameters μ and κ of the von Mises distribution describe the mean orientation (relative to the injection site) and the selectivity of the tuning, respectively, and they can be readily estimated from the vector average of the boutons' preferred orientations. We found that the mean orientations were close to those of the injection sites in both population cases (Fig. 7H, Table 2). For single cells, both mean orientation and orientation selectivity were scattered around the population values (Fig. 7H,I, Table 2) and showed no significant differences ($\mu_0: P = 0.34$, $\kappa_0: P = 0.61$, Student's *t*-test). The HWHH of the best-fit von Mises distributions is shown in Table 2.

Plots of the best-fit von Mises curves (Fig. 7B dotted lines) over the population data point out, however, that this mode alone is insufficient to account for the orientation distribution of the boutons. First, orientations around zero (relative to the site of origin) had a higher occurrence in the data than expected from the von Mises model (compare peaks in Fig. 7B), which might be the signature of the relatively high density of the local clusters. Second, the

shape of the curve could be influenced by the distribution of orientations in the entire map. If, for example, an orientation is overrepresented in the map, this could result in a corresponding bias in the orientation distribution.

In summary, the observed patterns suggest that similarity of spatial location and orientation preference between the source and target sites are major determinants of excitatory connection density. Nevertheless, in order to test this hypothesis we will have to take into account the joint effect of these variables, as well the structure of the orientation map.

Modeling functional topography at the population level

The effect of cortical distance and relative orientation on the density of boutons is demonstrated in the 2D histograms of the raw population data (Fig. 8A,B, center panels). These plots correspond to the empirical bouton density maps shown in Figure 5A,G, except that bouton numbers are pooled onto the axes of relative orientation and radial distance. In the following, we describe a mathematical model that gave good approximation of these bivariate density distributions. Then we consider the ability of this model to account for the patterns of single cells.

In the full, "two-component" version of the model we assumed that the density distribution of boutons in the cortical plane is a mixture of two independent components (Eq. 6): one that is selective both for nearby orientations and spatial locations ("oriented component") and another that is selective only for similarity of location ("nonoriented component"). The density of the oriented component

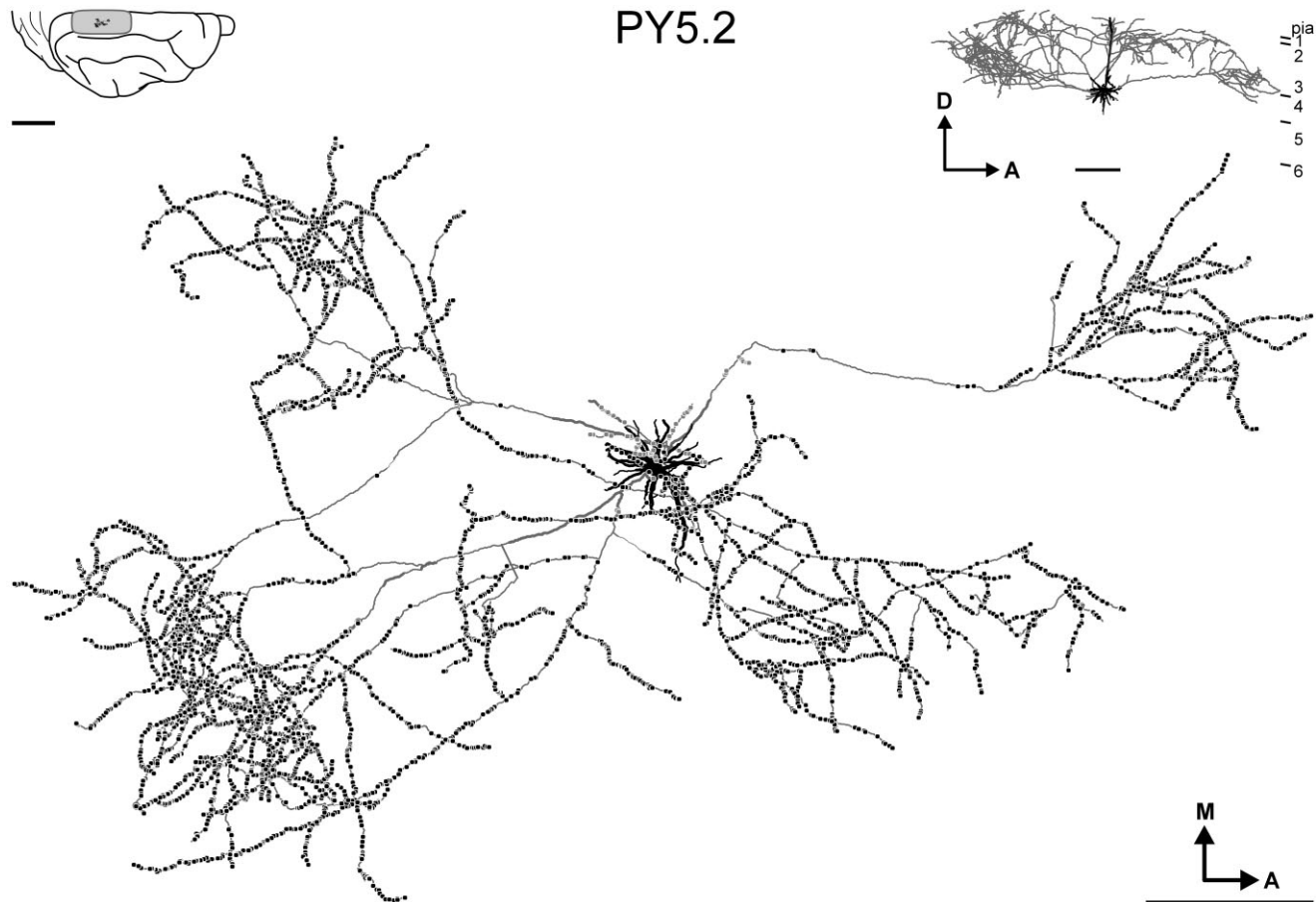


Fig. 4. Anatomical reconstruction of an intracellularly filled layer 5 pyramidal cell (cell PY5.2). The conventions are the same as in Figure 2. The majority of the axon (gray) formed extensively branching, patchy long-range lateral connections in the supragranular layers

while terminals were rare in the vicinity of the soma. Some axon segments were completely void of boutons while traveling to remote patches. A, anterior; L, lateral; D, dorsal. Scale bars = 500 μ m in reconstructions, 10 mm in cat brain inset.

was thus proportional to the joint probability of connections as a function of orientation and location, which were modeled by von Mises and Gaussian tuning functions (Eqs. 3, 4). The full model had five parameters: the width of the spatial distributions (σ_{21}, σ_{22}), orientation selectivity (κ_2), the relative preferred orientation (μ_2), and the weighting of the oriented component (m).

The generation of the model from its components is illustrated in Figure 5D–F (for Population 1) in the format of bouton density maps. Figure 8A (right-hand side) shows the bivariate distribution corresponding to the simulated map of Figure 5F. The goal of model optimization was to fit this bivariate model to the bivariate data distribution (center panel in Fig. 8A; see details in Materials and Methods).

The best-fit models (Fig. 8A,B, right-hand side) matched well the raw bouton distributions (Fig. 8A,B, center), accounting for 87% ($R^2_{2D} = 0.87$) of the variance in the case of Population 1 and 95% for Population 2. When collapsed onto the orientation axis, the model gave an excellent prediction of the orientation distribution of the raw data (left-hand side graphs in Fig. 8A,B; $R^2_{ori} = 0.98$ for Population 1, $R^2_{ori} = 0.99$ for Population 2). The radial distribution profiles were also well approximated (top graphs in

Fig. 8A,B; $R^2_{rad} = 0.92$ for Population 1, $R^2_{rad} = 0.98$ for Population 2). Indeed, the position and lateral extent of the major axon terminal patches was similar in the simulated (Fig. 5H,I) and the experimental 2D bouton density maps (Fig. 5A,G).

The presence of the nonoriented component was strongly suggested by the isotropic shape of the local bouton clusters (Fig. 5A,G). Indeed, when it was omitted from the model (“one-component model,” Eq. 5), this resulted in a poorer approximation of the spatial profile of the connections (gray broken lines in Fig. 8A,B, top panels; $R^2_{2D} = 0.87$ in the full vs. 0.71 in the one-component model for Population 1 and $R^2_{2D} = 0.95$ in the full vs. 0.89 in the one-component model for Population 2), confirming the inclusion of nonoriented connections in the model.

In order to test whether our model was significantly different from the experimental distributions, we performed a Monte Carlo simulation. We generated a set of “benchmark” R^2_{2D} values that would result if the same number of boutons were randomly drawn from a bouton density distribution perfectly corresponding to the best-fit full model (Fig. 5F,I). We obtained consistently higher R^2_{2D} values ($0.999 \pm 7.38 \times 10^{-5}$ for Population 1 and $0.999 \pm 1.28 \times 10^{-4}$ for Population 2, $P \ll 10^{-5}$ in both

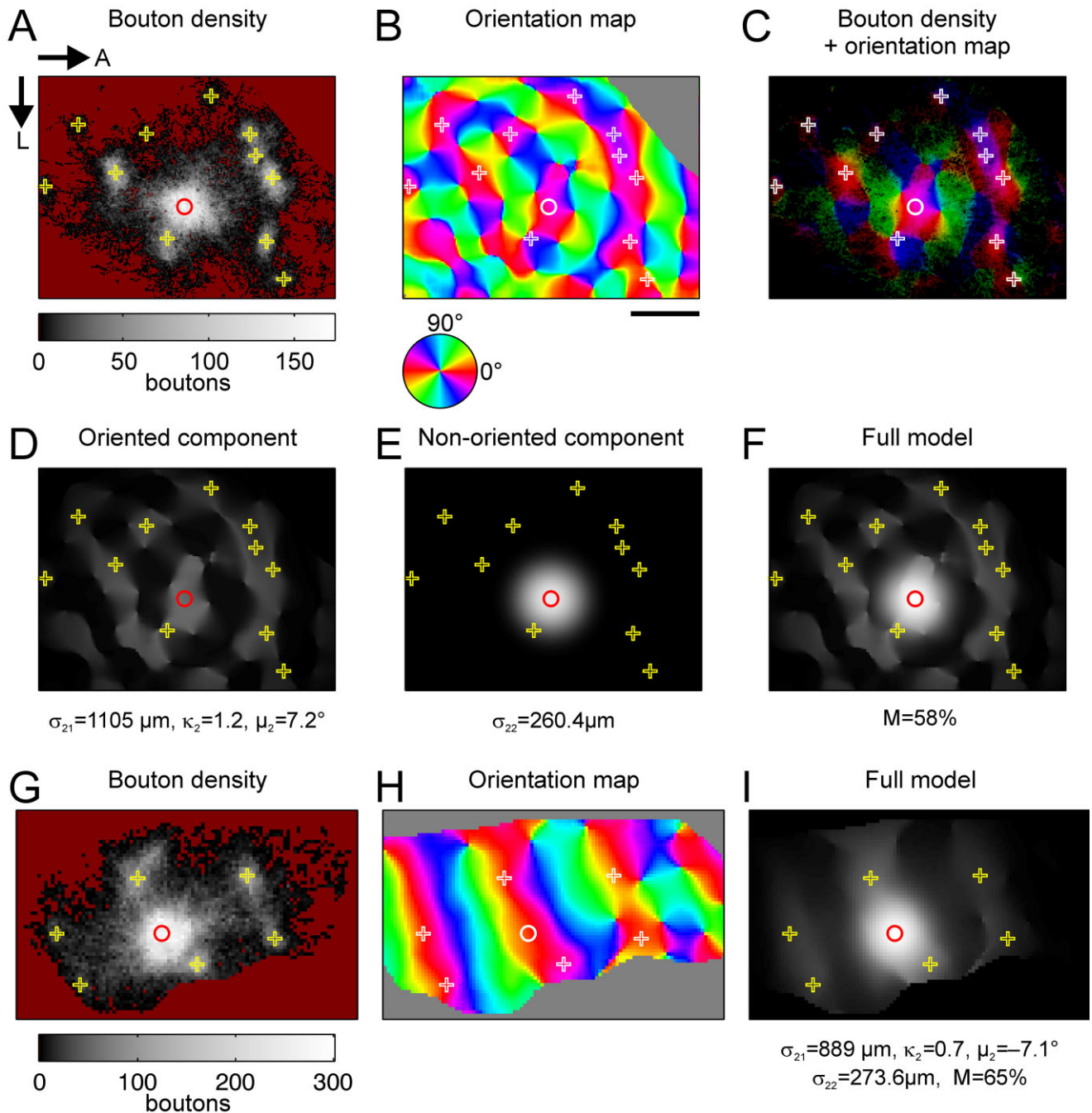


Fig. 5. Analysis of the population labeling in cortical layers 1–4 resulting from extracellular biocytin injections (**A–F**, Population 1, **G–I**, Population 2). The injection sites are marked by circles. Crosses show peaks of bouton density to assist comparison of the panels. **A:** The bouton density map of Population 1 shown on a gray scale. Brown background color denotes pixels with no boutons or orientation map, which were excluded from the analysis. **B:** Orientation map of the same area. Preferred orientation is color-coded according to the color wheel. The mask excluding regions from the analysis is shown in gray. **C:** The bouton density plot from **A** (zero and masked-out pixels shown in black) aligned with the orientation map from **B**. The central, dense portion of the labeling covers a broad range of orientations, while the remote patches are restricted to orientations similar to the center. **D–F:** The distribution obtained by fitting the full model to the raw data in **A**, as viewed in the cortical plane. The optimal model parameters are indicated under the maps (cf. Table 2). Note that it is the bivariate distribution (as a function of distance and orientation) of the boutons that was fitted (cf. Fig. 8A). Gray scale as in **A**, masked-out regions are black. **D:** The orientation-specific component of the model that accounted for 58% of the boutons in the model distribution. The connections close to the injection site follow the shape of the surrounding iso-orientation domain, which can also be recognized in the raw data in **A**. **E:** The isotropic (nonoriented) component of the model that describes well the central core of the labeling. This component accounts for 42% of the boutons in the model distribution. **F:** The full model, which is a sum of the oriented and nonoriented components corresponds well to the data ($R^2_{2D} = 0.87$, Table 2). For Population 2, the bouton density map (**G**), the orientation map (**H**), and the full model (**I**) are shown using the same conventions as in **A–F**. Arrows show anatomical directions, **A** anterior; **L**, lateral. Scale bar = 1 mm.

eters are indicated under the maps (cf. Table 2). Note that it is the bivariate distribution (as a function of distance and orientation) of the boutons that was fitted (cf. Fig. 8A). Gray scale as in **A**, masked-out regions are black. **D:** The orientation-specific component of the model that accounted for 58% of the boutons in the model distribution. The connections close to the injection site follow the shape of the surrounding iso-orientation domain, which can also be recognized in the raw data in **A**. **E:** The isotropic (nonoriented) component of the model that describes well the central core of the labeling. This component accounts for 42% of the boutons in the model distribution. **F:** The full model, which is a sum of the oriented and nonoriented components corresponds well to the data ($R^2_{2D} = 0.87$, Table 2). For Population 2, the bouton density map (**G**), the orientation map (**H**), and the full model (**I**) are shown using the same conventions as in **A–F**. Arrows show anatomical directions, **A** anterior; **L**, lateral. Scale bar = 1 mm.

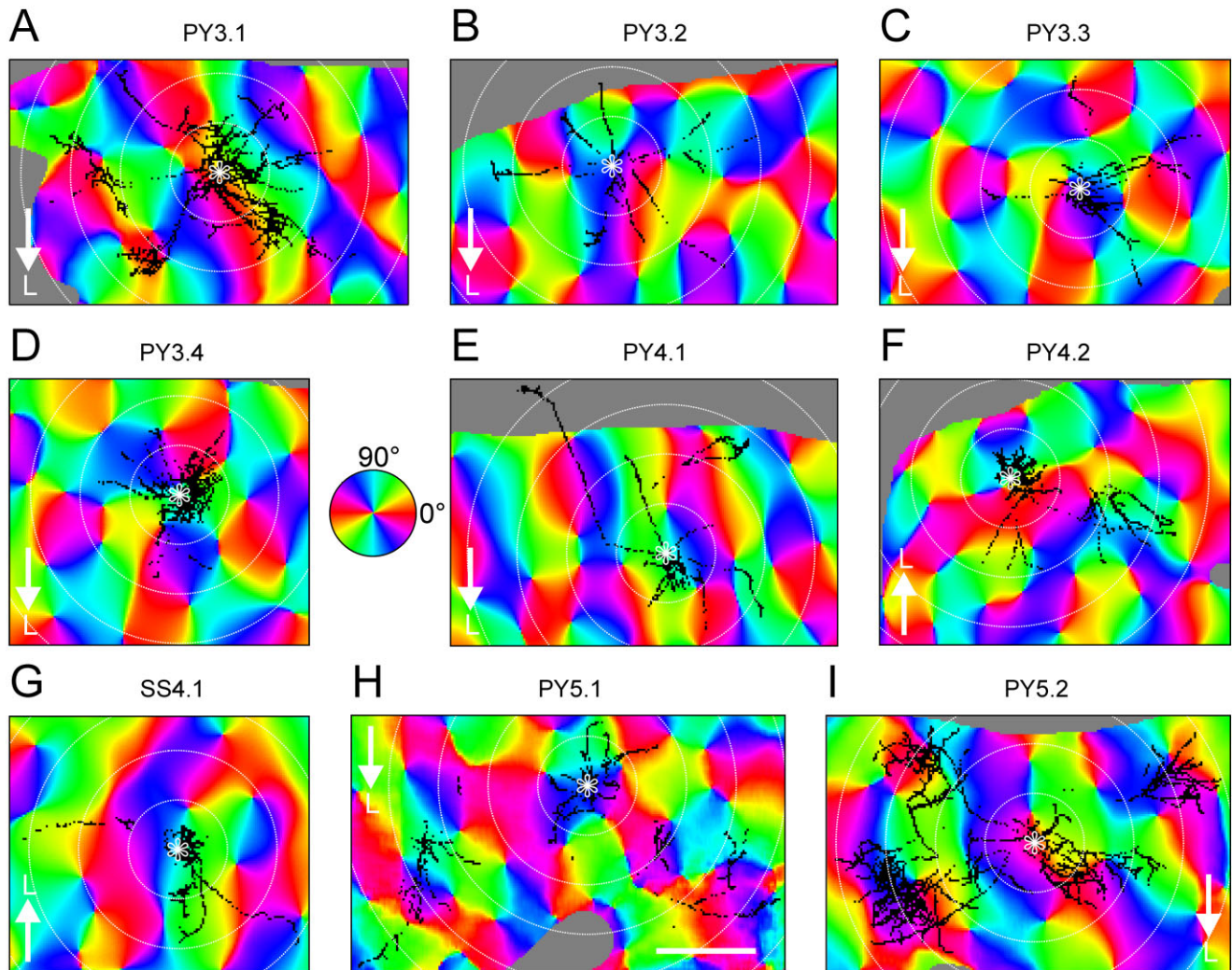


Fig. 6. The bouton distributions of the reconstructed single cells in the orientation map. **A–I:** The silhouettes of bouton distributions (black pixels) aligned with the orientation angle maps (coded according to the color wheel) of the corresponding area. Regions without

valid orientation map are masked out from the analysis (gray pixels). White circles show radial distance in 500- μ m increments from the soma (white asterisks). Arrows show lateral direction (L). Anterior is to the right. Scale bar = 1 mm.

cases, Student's *t*-test, $n = 100$ simulations each) than in the cases of real bouton density maps, although the difference was small (0.08 on average of the two cases). This result points out that, despite the good correspondence, the experimental bouton distributions contained a significant component not explained by the model.

The orientation maps of the population cases (Fig. 5B,H) represented two different types of map structure known from earlier descriptions (Shmuel and Grinvald, 2000). Case 1 had an apparently anisotropic organization with a regular pattern of orientation pinwheels. Case 2 was an example of "linear" organization, dominated by elongated regions of constant orientation preference. While lateral excitatory connections appeared to follow these different structures of the functional maps (Fig. 5A–C,G,H), some of the best-fit parameter values obtained for the two population cases were remarkably close to each other (Fig. 5D–F,I; Table 2). Accordingly, the width ratio of the oriented and nonoriented components ($\sigma_{21}:\sigma_{22}$) was

about 1:4–1:3. Also, the model allowed estimating the ratio of the boutons captured by these two components on the basis of their integral volumes (Eq. 7, see values of M in Table 2). According to this, more than half of the boutons belonged to the orientation-specific component of the model, which represented the patchy connections. The orientation preference of this component (μ_2), responsible for the location of the patches, was only about 7° different from that of the injection sites (Table 2) and the HWHH of the underlying von Mises function was on average 39.2° (Table 2). These findings suggest that lateral connections formed under similar constraints can underlie different map structures.

Pooled single cells as a population

Although the single cells in this study were obtained from areas 17 and 18, where visuotopic and orientation maps are believed to be organized according to the same principles (Tusa et al., 1978, 1979; Cynader et al., 1987;

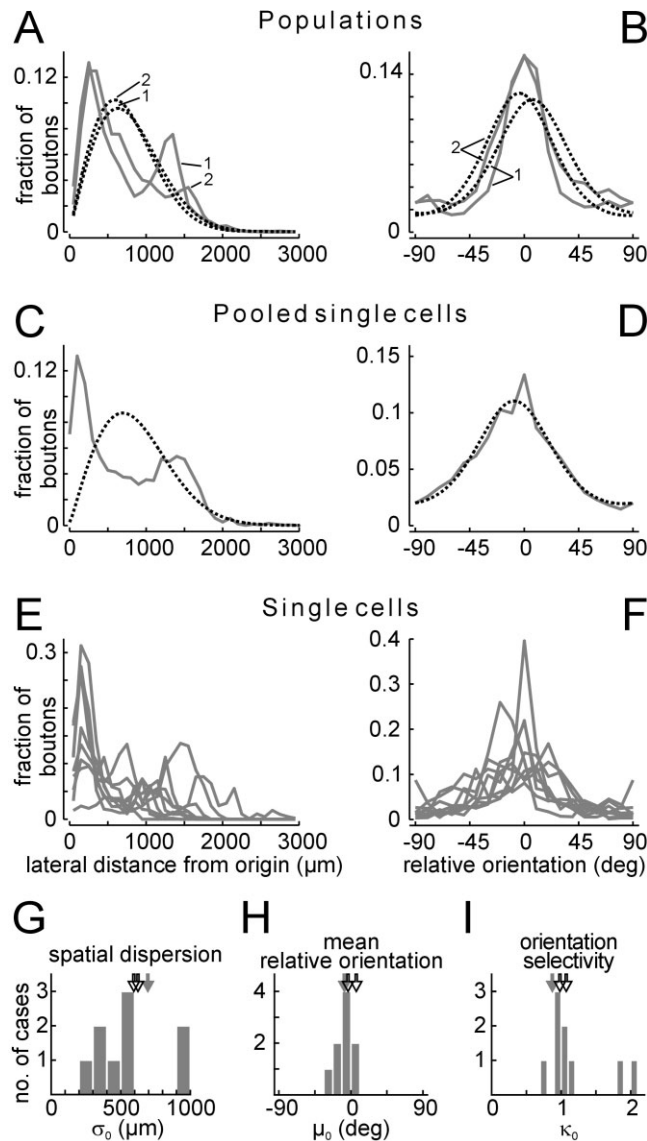


Fig. 7. Radial and orientation distribution of the boutons. The distribution of raw bouton data is shown by the gray lines. **A,C,E:** The fraction of boutons against distance from the site of origin (bin size 100 μm). **B,D,F:** The fraction of boutons against orientation preference (bin size 10°) relative to the orientation of the site of origin (0°). **A,B:** Data of the population cases (identified by numbers) shown in Figure 5A,G. The radial distribution (A) of the boutons would be expected to follow the Rayleigh distribution (dashed black lines) if the bouton density distributions (Fig. 5A,G) were isotropic 2D Gaussians centered on the corresponding injection sites. Compared to this simple model, there are additional peaks in the raw data due to clustering of the boutons. The orientation distributions (B) resemble the best fit von Mises distributions (dashed black lines) obtained by maximum likelihood estimate of parameters μ and κ (see Materials and Methods for details). **C,D:** Pooled data of the nine reconstructed single cells. Dashed black lines show the best-fit statistical distributions as in A and B, respectively. Both the radial (C) and orientation (D) distribution of the boutons resemble those of the population cases, suggesting that the single cells are drawn from a population organized in a similar way. **E,F:** The overlaid radial (E) and orientation (F) distribution profiles of the nine reconstructed single cells. **G–I:** Distribution of the parameter values characterizing the spatial dispersion (σ_0 , G), mean relative orientation (μ_0 , H), and orientation selectivity (κ_0 , I) of population and single-cell bouton distributions. The values correspond to the best-fit Rayleigh or von Mises distributions, such as those shown in A, C or B, D, respectively. Histograms, single cells; open black arrows, populations; filled gray arrows, pooled single cells.

Bonhoeffer et al., 1995; Buzás et al., 2003), they were labeled from different injections, hemispheres, or animals. It is thus reasonable to ask whether they constitute a representative sample of a network that is organized in the same fashion as the population cases. In order to test this question, we pooled the radial distance and relative orientation data pairs of the boutons of all single cells (Fig. 8C, middle panel). The radial and orientation distribution of the population cases and the pooled single cells (Figs. 7C,D, 8C) shared most characteristic features. Indeed, in plots of the estimated model parameters, such as spatial dispersion, relative preferred orientation, orientation selectivity (Figs. 7G–I, 10A–D), and the relative size of the oriented and nonoriented components (Fig. 10E), the pooled single cells and the population cases clustered tightly together. Finally, the fit of the full model to these combined data was almost as good as for the populations ($R^2_{2D} = 0.83$; Figs. 8C, 10A, Table 2), suggesting that our single cell sample was representative.

Diversity in the lateral connections of excitatory neurons

We have shown in the previous sections that excitatory lateral connections can be described at the population level by a combination of orientation-specific and nonoriented connections, both of which follow simple tuning functions. The question then arises whether individual constituents of such neuronal populations follow the same rules. If this was the case, the single cells could be sufficiently approximated by the population model and could thus be regarded as instances of the population distributions simply “scaled down” in the absolute number of axon terminals.

In order to test this, we performed least-squares fitting of the full model to the bouton distributions of the single excitatory neurons reconstructed. The numerical results are shown in Table 2. Notably, R^2_{2D} values expressing the goodness of fit varied over a broad range (0.31–0.90), some cells being close to the population cases, although the majority was smaller (median $R^2_{2D} = 0.68$). For three representative examples, the experimental and best fit model distributions are illustrated in detail in Figure 9 (same cells as in Figs. 2–4).

Which features of the single cell distributions could then account for this difference? As boutons are discrete (quantal) entities and their number per neuron is about 10–100 times less than in the population cases (Table 1), this could impose an upper limit on the variance that can be explained by the smooth tuning functions of the model. We tested this by simulating datasets, which comprised the same number of boutons as the real cells (using the Monte Carlo protocol described above for the population cases) but precisely followed the best-fit model. The R^2_{2D} values obtained for these datasets were always larger (on average by 0.31 ± 0.20 , $P < 10^{-5}$, Student's *t*-test, $n = 100$ simulations per cell), meaning that the smaller number of boutons in the single cells alone could not account for the observed decrease in goodness of fit.

Local fluctuations in bouton density or “clumping,” which could, for example, result from constraints of the tree-like axonal morphology, is another potential source of residual error. As long as such fluctuations are random, they are expected to diminish when the number of data dimensions we wish to model is decreased. Supporting this notion, we found that the R^2 improved significantly

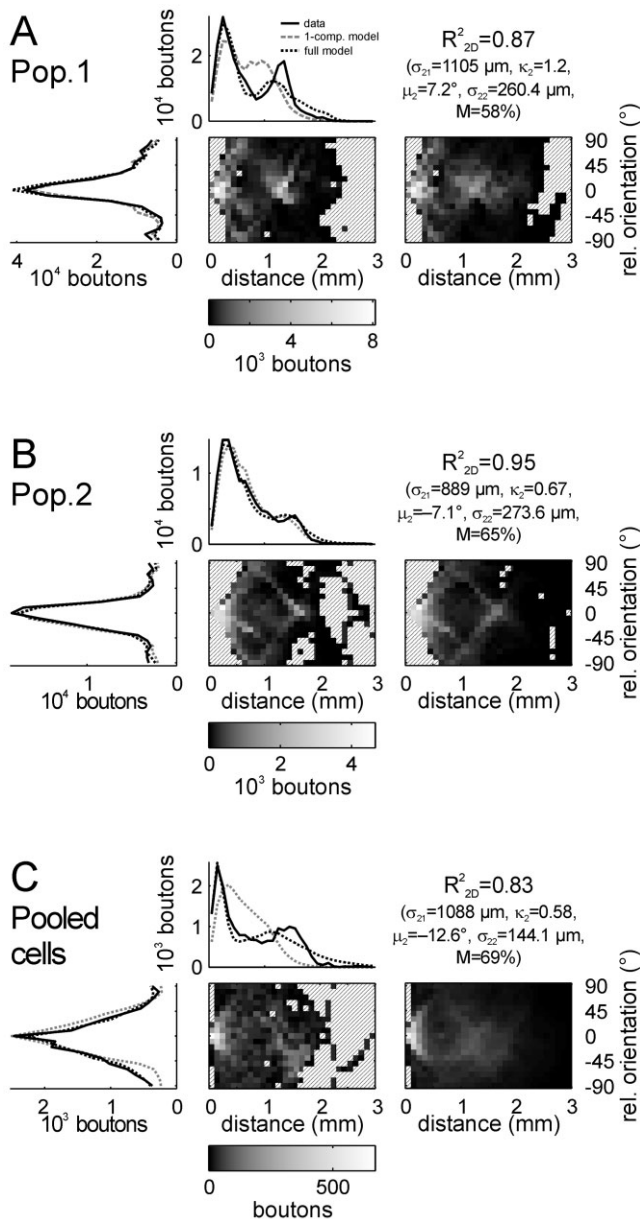


Fig. 8. Modeling of the bivariate (orientation and radial) distribution of boutons from two population labeling experiments (**A,B**) and from the pooled data of the nine individually reconstructed excitatory neurons (**C**). In each panel the gray-scale-coded 2D histograms show the bivariate distributions of labeled boutons in the raw data (middle) and the best fit model distribution (right-hand side) as a function of distance from the site of origin and relative orientation preference of the target sites. The color-code is shown at the bottom, striped background denotes bins with no boutons. Line plots show the (univariate) distributions as a function of distance (top) and orientation preference (left-hand side), respectively. Solid lines, raw data; dotted gray lines, best-fit one-component model; dotted black lines, best-fit full model. The full model gives a good approximation of the experimental distributions in each case ($R^2_{2D} = 0.87$ in **A**, 0.95 in **B**, and 0.83 in **C**). The optimal model parameters are indicated at the top right (cf. Table 2). Bin size is $100 \mu m$ for distance and 10° for orientation.

(Fig. 10A–C; paired *t*-test, $P = 0.0032$ for R^2_{rad} , $P = 0.0081$ for R^2_{ori} , single cell cases only), when boutons were pooled onto the radial distance or relative orientation axes (Fig.

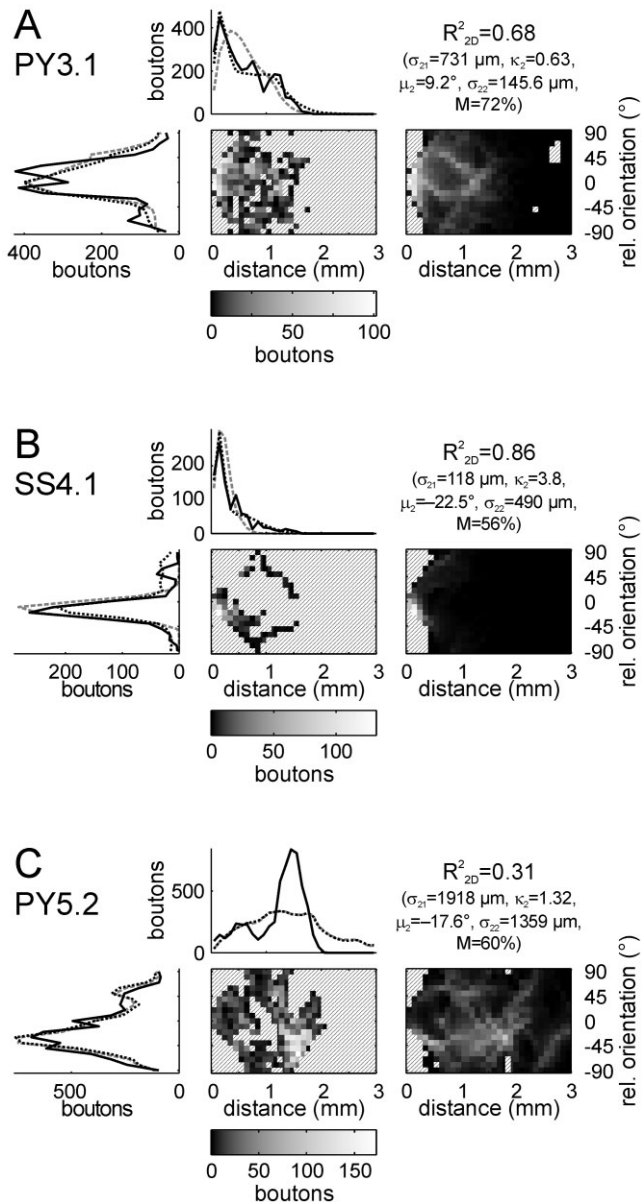


Fig. 9. Modeling of the bivariate bouton distributions of three excitatory neurons shown in the same format as in Figure 8. The anatomical reconstructions of these cells are shown in Figures 2–4 and their bouton distributions and orientation maps are shown in Figure 6A,G,I, respectively. **A:** The bouton distribution of pyramidal cell PY3.1 is relatively well predicted by the model ($R^2_{2D} = 0.68$). **B:** Spiny stellate cell SS4.1 showing highly asymmetric local connections (Fig. 6G). The asymmetry is well explained by the model as a shift of orientation preference by 22.5° from that of the soma location ($R^2_{2D} = 0.86$). **C:** Pyramidal cell PY5.2 showing very sparse local connections. This feature is unexpected by the model and results in a poor fit in general ($R^2_{2D} = 0.31$). The orientation distribution (left) is, nevertheless, relatively well predicted ($R^2_{ori} = 0.78$).

9A–C, line graphs). The graphs also illustrate that secondary peaks or skewed shape of the orientation distributions were occasionally well captured (Fig. 9A–C, left-hand side), and thus they do not, per se, invalidate the simple principles of the model.

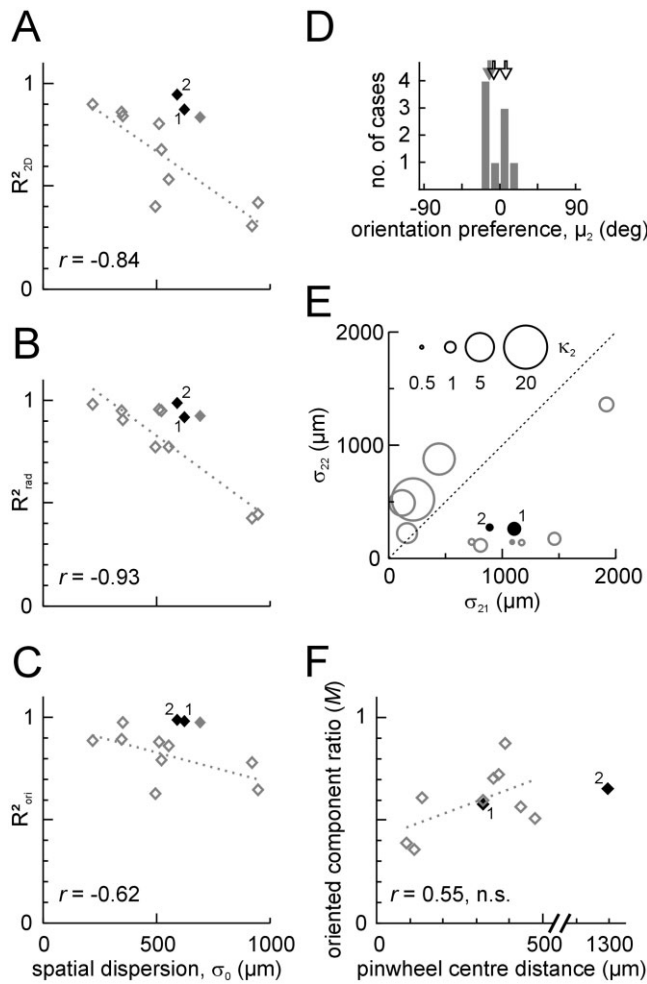


Fig. 10. Single cells show large variability in their compliance to the model. Solid black symbols, population cases (identified by numbers); open gray symbols, single cells; solid gray symbols, pooled single cells. **A–C:** The model's goodness of fit is negatively correlated with the spatial dispersion σ_0 of boutons. Scatterplots show the dependence of the R^2 values of the model's bivariate (A) and univariate radial (B) and orientation (C) distributions. Pearson's correlation coefficients and regression lines are shown for the single-cell cases. The dependence of the model fits on spatial dispersion is stronger for the radial distribution (B) than for the orientation distribution (C). For the populations and pooled cells, the model always performs better than the trend of single cells. **D:** Histogram showing the distribution of the preferred orientations of the oriented components (μ_2) estimated by fitting the full model to the single-cell data. The values are scattered around similar estimates obtained for the population cases (open black arrows) and the pooled single cell data (filled gray arrow). **E:** Comparison of the spatial extent of the oriented (σ_{21}) and nonoriented (σ_{22}) components and the orientation selectivity (κ_2 , see legend in inset) as estimated by fitting the full model. Single cells fall into two main groups: those with $\sigma_{21} < \sigma_{22}$ whose oriented component was more orientation selective (κ_2 higher). Larger cells had $\sigma_{21} > \sigma_{22}$ and broader orientation selectivity (κ_2 lower), similar to the populations and pooled cells. **F:** The estimated amount of orientation-specific connections shows no significant correlation with the distance of the soma from the nearest pinwheel center. Pearson's correlation coefficient and regression line shown for the single-cell cases.

The best model fits were obtained for the cells possessing more locally concentrated axon arbors. This is shown by the negative correlation of R^2_{2D} values with the spatial

dispersion (σ_0) of the boutons ($r = -0.84$; Fig. 10A). The analysis of one of the largest cells in the sample (case PY5.2; Fig. 9C) illustrates that for greater cells the relatively good fits of the orientation distributions ($r = -0.62$ for R^2_{rad} ; Fig. 10C) were accompanied by radial distribution profiles often inconsistent with the model of soma-centered Gaussians ($r = -0.93$ for R^2_{rad} ; Fig. 10B). Importantly, the model always performed above this trend for the population data as well as the pooled single cells (filled symbols in Fig. 10A–C).

Figure 10D,E summarizes the range of behaviors of the model and compares populations and single cells (also see Table 2). The relative orientation preference of the oriented model component (μ_2 ; Fig. 10D) covered a range of about $\pm 20^\circ$ and it was not statistically different from the mean orientation of the boutons (μ_0 ; Fig. 7H; $P = 0.95$, paired *t*-test for all cases). We found no correlation between any of the model parameters and the (unsigned) relative orientation preference of the connections.

In the case of some cells with more locally concentrated connections (such as the spiny stellate cell, Fig. 9B, and some pyramidal cells, see Table 2), the oriented component was estimated to be smaller than the nonoriented component. This was accompanied by a narrow orientation selectivity (κ_2 higher), consistent with the structure of the orientation map, which offers a narrower range of orientations locally. Conversely, the oriented component of spatially more dispersed cells was more extensive in space ($\sigma_{21} > 500 \mu\text{m} > \sigma_{22}$) as well as orientation (κ_2 smaller). The parameter estimates of most of these large cells clustered together with the population cases (black markers in Fig. 10E).

Influence of pinwheel centers

A possible reason for the variability in single-cell connection patterns is their different distance from pinwheel centers. Pinwheel centers are singular points of the cortical orientation map where all orientations are represented within a short distance (Swindale et al., 1987; Bonhoeffer and Grinvald, 1991). Yousef et al. (2001) found that tracer-labeled populations of lateral connections originating from these regions show more uniform distribution of orientations than connections of orientation domains. In terms of the present study, one would expect that this center-type connectivity corresponds to a decreased ratio of oriented connections, i.e., in the ratio M (Eq. 7, Table 2). Figure 10F shows a comparison of the estimated ratio of oriented connections and the distance of the cell bodies from the nearest pinwheel center (as identified by visual inspection of the angle maps). Although cells with lower M tended to be closer to pinwheel centers, the correlation was not significant throughout the single cell cases ($r = 0.55$, Pearson's correlation). It should be noted, however, that in our sample the distances were mostly larger (average 390 μm , range 90–1290 μm , including population and single cell cases) than in the above study (Yousef et al., 2001), where injections were placed up to 100 μm from the nearest pinwheel center.

Estimating the effect of the dendritic placement of boutons

It is known that the vast majority of excitatory synapses is located on the dendrites of target neurons (Kisvárdai et al., 1986; Gabbott et al., 1987; McGuire et al., 1991), and thus a bouton can be up to several hundred μm away from

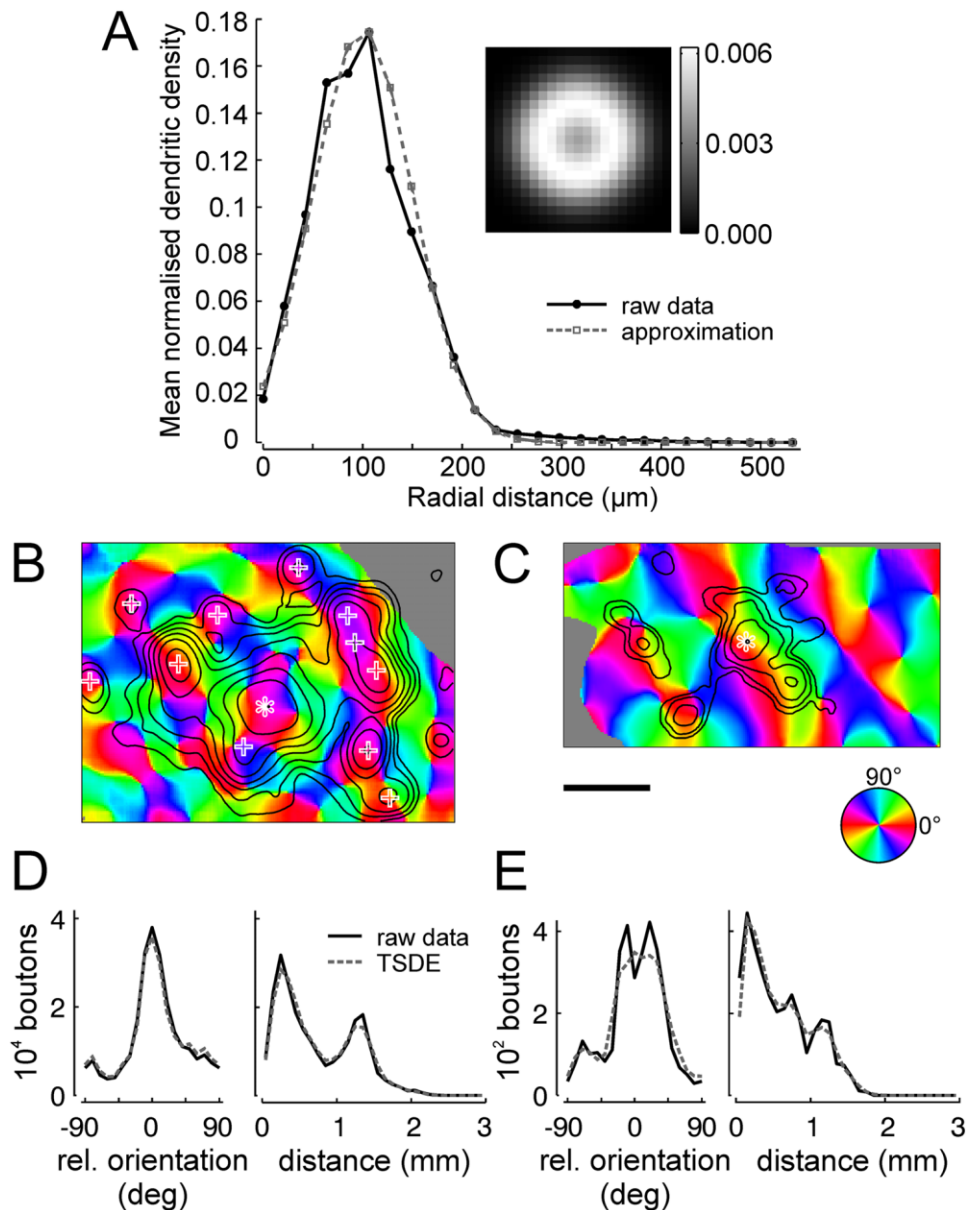


Fig. 11. **A:** Radial distribution of normalized dendritic density based on measurement of 28 pyramidal cell dendritic trees (raw data, black) and its approximation by a Gaussian distribution with a mean = 100 μm and SD = 50 μm (approximation, gray). Revolving this profile around the ordinate and normalizing the resulting integral volume created the annular kernel shown in the inset. **B,C:** Target soma density estimate (TSDE) maps of case Population 1 (B) and the pyramidal cell PY3.1 (C) were obtained by convolving the raw

bouton density maps (see Figs. 5A, 6A, respectively) by the kernel in A. Black lines indicate isodensity levels at 1/1, 1/2, 1/4, 1/8, 1/16 (for C,D) and additionally 1/32, 1/64, and 1/128 (for C) of the maximum. White asterisks, centers of origin; white crosses, approximate positions of patches (same as in Fig. 5A). **D,E:** Comparison of the orientation and radial distributions of the raw (black solid lines) and TSDE maps (gray dashed lines) show no substantial difference. Scale bar = 1 mm in C.

the target soma. This positional offset means that the synaptic effect of the axon could reach target neurons whose preferred orientation is different from that determined at the site of the bouton. To what extent might our findings be affected by this issue? To answer this question, we considered a 2D spatial kernel (Fig. 11A, inset) corresponding to the estimated probability density of postsynaptic somata around a bouton. We designed this kernel using measurements of dendritic density of 28 recon-

structed pyramidal neurons as a function of distance along the cortical surface (see Materials and Methods). The density distribution of dendrites had its peak about 100 μm from the cell body, implying that boutons are located at this distance from postsynaptic target somata with maximum probability (Fig. 11A). The raw bouton density maps were then convolved with the kernel to produce what we refer to here as target soma density estimate (TSDE) maps.

The TSDE maps were analyzed similarly to the raw bouton density maps. Figure 11B-E illustrate that replacing bouton position with the probability distribution of the postsynaptic somata resulted in smoothing the connectivity map. Nevertheless, this caused only a minor (although significant) increase in spatial dispersion (change in σ_0 from raw to TSDE maps: $8.6 \pm 7.2 \mu\text{m}$, mean \pm SD; $P = 0.0042$; all statistical tests reported in this section are paired t -test, $n = 10$) and orientation selectivity (change in κ_0 from raw to TSDE maps: -0.2 ± 0.1 , $P = 1.2 \times 10^{-4}$). The mean orientation angle was statistically the same in the TSDE and raw bouton density maps.

Since the smoothing effect of the kernel decreased the variance in the distribution of connections, we found an improvement of the goodness of the fit obtained for the full model as compared to the raw maps (average increase in R^2_{2D} 0.13 ± 0.09 , $P = 9.2 \times 10^{-4}$), but none of the best-fit model parameters showed statistically significant change. We thus conclude that the potential positional offset between the location of boutons and the somata of their target cells did not significantly influence our results.

DISCUSSION

The correlation between functional maps and long-range intrinsic connections has been assumed ever since their discovery (Mitchison and Crick, 1982; Rockland and Lund, 1982; Gilbert and Wiesel, 1983). Theoretical investigations have corroborated the idea that lateral connections have an important bearing on the large-scale spatial organization of sensory representation in primary sensory cortices (Willshaw and von der Malsburg, 1976; Xing and Gerstein, 1996; Adorján et al., 1999; Shouval et al., 2000; Ernst et al., 2001; Carreira-Perpiñán and Goodhill, 2004; Blumenfeld et al., 2006). Here we studied the relationship between orientation maps and the spatial organization of intrinsic excitatory connections in the cat primary visual cortex. We show that large populations of lateral connections can be modeled quantitatively as a mixture of orientation specific and nonspecific components that follow tuning functions of cortical position and orientation. Individual neurons, when treated as a population, follow the same principles. However, when analyzed separately their connection patterns can only be partially explained by these general rules. We also demonstrate that our results are not significantly affected by the positional offset between the presynaptic boutons and postsynaptic somata.

Simple tuning model explains population-level connectivity

One novelty of the present study is that we introduced a simple, mathematical formalization with which the joint spatial (radial) and orientation distribution of large populations of boutons could be described and numerical estimates of their underlying tuning functions could be extracted.

The types of tuning functions incorporated in the model are often used to describe RF tuning properties. Their use here can be substantiated as follows. In order to model the orientation distribution of synaptic boutons, we made the assumption that the probability of a neuron's axon synapsing with other neurons is proportional to the probability of that neuron responding to the preferred orientation

of the target. Hence, the orientation distribution of the connections was expected to follow the shape of a general orientation tuning function. We used the von Mises function for this purpose because it has been recently shown to be an optimal model for the orientation tuning of single unit and optical responses (Swindale, 1998; Swindale et al., 2003).

For modeling the spatial distribution of connections, 2D Gaussians were applied, which is supported by two main lines of experimental findings. First, it is known that the spatial envelope of visual cortical RFs can be well characterized by 2D Gaussian functions (Jones and Palmer, 1987). Following assumptions made for the orientation distribution above, we expected that the distribution of RF locations of the neuron population targeted by a given cell is also proportional to the spatial envelope of the presynaptic RF. Moreover, assuming that the visuotopic map is locally linear (Warren et al., 2001; Bosking et al., 2002; Buzás et al., 2003; Yu et al., 2005), this target population RF converts into a Gaussian on the cortical surface. Second, it seems plausible that the shape of the cortical point spread function, which can be well approximated with the 2D Gaussian (Cynader et al., 1987; Grinvald et al., 1994; Das and Gilbert, 1995), is determined by the excitatory lateral connections that originate from a single cortical locus.

Despite the fact that about 90% of the variance in the joint radial and orientation distribution of excitatory connections was accounted for by the full model, our calculations also showed that a significant proportion remained unexplained. This is not surprising in light of the many factors that may influence the layout of the lateral intracortical network. For example, previous studies have found functionally relevant anisotropies in the distribution of lateral connections (tree shrew: Bosking et al., 1997; cat: Schmidt et al., 1997; owl monkey: Sincich and Blasdel, 2001; but see Angelucci et al., 2002, for differences in the macaque). These are, on the one hand, due to unequal cortical magnification along the horizontal and vertical visual field dimensions (Tusa et al., 1978, 1979; Cynader et al., 1987; Yu et al., 2005). Superimposed on this anisotropy, the target population RFs may also reflect the elongation of cortical RFs (Mooser et al., 2004) and collinear interactions between adjacent RFs (Kapadia et al., 1995; Chisum et al., 2003).

Furthermore, correlation-based development of intracortical connections predicts that the probability of two cortical locations to be linked should increase with the similarity of the RF properties represented at those locations (Callaway and Katz, 1991; Löwel and Singer, 1992; Miller, 1994; Erwin and Miller, 1998). This should be detectable at the spatial resolution of our method for those RF properties that have map-like distributions, including visuotopy (Hubel and Wiesel, 1962; Tusa et al., 1978, 1979), direction preference (Shmuel and Grinvald, 1996), ocular dominance (Tieman and Tumosa, 1983; Hübener et al., 1997), and spatial frequency (Tootell et al., 1981; Hübener et al., 1997; Sirovich and Uglesich, 2004). A detailed knowledge of the relevant maps would potentially allow modeling their effects on anatomical connectivity, but only at the cost of a radical increase in the number of model parameters. An alternative, spatiotemporal energy model of functional map organization has been suggested recently (Basole et al., 2003; Mante and Carandini, 2005), which was shown to unify some of the previously known

feature maps. Thus, a perhaps more elegant connectivity rule could be based on similarity of spatiotemporal energy instead of specific map features.

Functional specificity of local connections

Our full model incorporated two independent Gaussian components, one that limited the spatial spread of orientation-specific connections and another, nonoriented one. This approach is in line with the result of a recent *in vitro* optical imaging study of layer 2/3 of ferret visual cortex (Tucker and Katz, 2003) suggesting that excitation spreads within a few hundred μm from focal intracortical activation sites in an isotropic fashion, while outside this region clusters of activity can be observed. Furthermore, studies by Bosking et al. (1997) and Malach et al. (1993) using combined optical imaging and anatomical tracing found that the orientation specific relationship of lateral connections with orientation maps only exists outside an approximate distance of 400–500 μm from the injection site, but more proximal connections are not orientation-specific.

We should emphasize here that it is ambiguous whether local connections correlate with similarity of orientation or similarity of location because these variables are themselves highly correlated within a cortical hypercolumn. Therefore, we assumed that orientation-specific and purely location-specific connections are superimposed and searched for the best estimate of their sizes and contributions to the entire connection pattern. Our calculations for the population label showed that the nonoriented component was restricted within a few hundred μm around the injection site (Fig. 5E,I, Table 2), whereas the oriented component extended 3–4 times further.

The same correspondence between “local” and “nonoriented” connections could not be made for single cells. The local connections of individual neurons appeared asymmetric and, occasionally, very sparse (Figs. 2–4, 6). Furthermore, model estimates of the size and contribution of the nonoriented component varied greatly among the single cells (Fig. 10E, Table 2). These findings suggest that individual neurons generally do not form functionally homogeneous local connections. Supporting this notion are reports by Roerig and colleagues (Roerig and Kao, 1999; Roerig and Chen, 2002; Roerig et al., 2003). Those authors used the technique of *in vitro* laser photostimulation in ferret primary visual cortex to map the presynaptic cells that provide excitatory input to single visual cortical neurons and found functionally specific and anatomically anisotropic spatial distributions. Indeed, recent simulation studies (Adorján et al., 1999; Shouval et al., 2000) demonstrated that locally anisotropic intracortical connections can provide the basis for orientation tuning in biologically realistic networks (but see Angelucci et al., 2002).

How, then, can the presence of nonspecific local connections in population labeling patterns be explained? On the one hand, the asymmetric local connections of individual neurons could reflect their preference for functionally defined subsets of the surrounding neurons. In this case we have to assume that the connectivity rules of neighboring neurons that define these connections are uncorrelated, so that their summation in an extracellular labeling experiment results in a symmetrical distribution. Alternatively, the anisotropic core region of anatomical connectivity could simply result from nonspecific spread of the tracer substance. The analysis presented here allows for this component to be discounted, but resolution to the question

will ultimately require mapping the synaptic connections of multiple neighboring neurons.

Orientation preference and selectivity of lateral excitatory connections

Previous experimental studies agree that lateral connections prefer similar orientations to the site of origin (Gilbert and Wiesel, 1989; Malach et al., 1993; Kisvárday et al., 1994, 1997; Bosking et al., 1997). Simulation studies suggest that this is a signature of the cortical network that reinforces (Ben-Yishai et al., 1995; Somers et al., 1995; Vidyasagar et al., 1996) or, indeed, creates orientation tuning (Adorján et al., 1999; Ernst et al., 2001) as well as maintains the map of stimulus orientation (Weliky and Katz, 1994; Koulakov and Chklovskii, 2001; Carreira-Perpiñán and Goodhill, 2004; Blumenfeld et al., 2006). The present study provides numerical estimates of the orientation preference and selectivity of the anatomical connections, which are critical parameters of most models of visual cortex organization.

Our method relies on the correct measurement of orientation preference over large cortical regions. Similar to a range of earlier studies (Malach et al., 1993; Kisvárday et al., 1994; Weliky et al., 1995; Bosking et al., 1997, 2000; Buzás et al., 1998, 2001; Yousef et al., 2001; Mooser et al., 2004), we achieved this using the technique of optical imaging, which has been demonstrated to reflect the average orientation tuning of underlying neurons (Shmuel and Grinvald, 1996). We should note, however, that the fact that optical imaging measures a population response also introduces some uncertainty in determining the preferred orientation of individual neurons, as discussed below.

Our results agree with the above experimental studies as far as the preferred orientation of large populations of excitatory connections was only slightly different from those of their sites of origin (Figs. 7B,H, 8A,B, Table 2). But we also demonstrated that the smooth, unimodal iso-orientation tuning of the overall anatomical connectivity is a collective effect of neurons, whose orientation distributions show individual deviations from that of the population.

Nevertheless, each neuron approached a unimodal orientation tuning when the entire cell was taken into account (left-hand side graphs of Fig. 9, Fig. 10A,C). The estimated peak orientation of the single cell connections was found to be variable within a range of about $\pm 20^\circ$ (Figs. 7H, 10D) relative to the optically imaged orientation preference of the soma location. This may suggest a preference for dissimilar orientations, although that possibility remains indistinguishable from the alternative of orientation scatter. It is known from electrophysiological recordings that neighboring neurons may have different preferred orientations, for example, due to the presence of pinwheel centers (Swindale et al., 1987; Bonhoeffer and Grinvald, 1991; Maldonado and Gray, 1996; Maldonado et al., 1997; Buzás et al., 2003) or other factors (Lee et al., 1977; Bishop, 1979; Hetherington and Swindale, 1999). These individual differences do not appear in the optical response, which reflects the average orientation preference of many neurons (Shmuel and Grinvald, 1996).

The present analysis also shows that the tuning half-width of anatomically detectable excitatory connections in the intrinsic network is on the order of 30–40° (HWHH, Table 2). These values are comparable to the tuning width of the intrinsic optical signal, as measured by Swindale et

al. (2003) using a similar model-based method (see their fig. 3c). This is compatible with our findings, since the orientation distribution of lateral connections is expected to determine the tuning of incoming presynaptic spikes and resulting subthreshold electrical activity at any cortical locus. Such electrical activity is known to be reflected in the intrinsic signals (Grinvald et al., 1994; Toth et al., 1996; Takashima et al., 2001; Petersen et al., 2003).

The orientation tuning width of intracortical excitation is also likely to be a major determinant of each target neuron's response characteristics (Creutzfeldt et al., 1974; Ferster, 1986; Douglas et al., 1991; Peters and Payne, 1993; Volgushev et al., 1993; Ahmed et al., 1994; Somers et al., 1995; Monier et al., 2003). Roerig and Chen (2002) measured intracellularly the orientation tuning of postsynaptic potentials of intracortical origin and reported an average tuning width of 19°, thus lower than that expected from our anatomical data. This points toward mechanisms sharpening the effect of cortical excitation on the somatic membrane potential, which may include concurrent, broadly tuned inhibition (Hata et al., 1988; Bonds, 1989; Somers et al., 1995; Buzás et al., 2001; Roerig and Chen, 2002; Roerig et al., 2003), feed-forward thalamic input (Ferster and Miller, 2000), as well as other cellular mechanisms (Volgushev et al., 1993; Pei et al., 1994; Volgushev et al., 2000; Monier et al., 2003).

Implications for physiological diversity

The results from the present functional-topographical analysis of single-cell axonal fields raise two important questions. First, why was the population model generally insufficient to fit the distribution of these connections? And second, what is the functional relevance of the variability in the estimated spatial and orientation tuning parameters of single neurons?

Before discussing these aspects further, we should consider to what extent potential incomplete labeling or reconstruction of the axons could have contributed to the observed intercell variability. Under the assumption that such artifacts were independent of lateral direction, their effect on the analysis would have been largely mitigated since we pooled all axonal projections onto the radial distance axis before fitting the model. Furthermore, we found that the largest cells diverged most strongly from the population model (Fig. 10A–C), suggesting that technical limitations could have covered even further diversity.

We measured the compliance of the experimental bouton distributions to the model using R^2 values, which quantify the proportion of variance explained. One possibility why the residual variance might remain relatively high after model optimization is if random local fluctuations of bouton density are superimposed on an otherwise model-conform relationship. Such “clumping” of boutons can easily result from the constrained cellular morphology, where boutons are arranged along the axon tree and on the target cell's dendritic and somatic surfaces. As we have seen in the analysis of TSDE maps, smoothing the bouton density maps indeed reduced the fit error. Model fits also improved when boutons of a cell were pooled either onto the orientation or the distance axis (Fig. 9, line graphs), suggesting that some subcellular differences do balance out when the entire cell is taken into account (Fig. 10B,C). Nevertheless, these univariate distributions were still more difficult to fit than those of the populations (Fig. 10B,C) and the best-fit model parameters of the single

cells varied widely around the population values (Fig. 10D–F). The latter two facts indicate that deviations from the population connectivity pattern were not simply due to random fluctuations of bouton density.

Our results complement, from a functional perspective, a previous study using 3D reconstruction of the overlapping axonal fields of 10 pyramidal cells that were labeled from the same injection site (Kisvárday and Eysel, 1992). These neurons showed a rich variation in the axonal connectivity, whereas superimposition of all 10 axons resulted in a stereotyped patchy pattern. Similarly, the present data are compatible with the view that any individual neuron connects only to a subset of those targets that are reached by the entire population of cells at the same cortical site. In this way, the sparse connectivity can enrich functional diversity even in closely spaced neurons. Further support for this recognition comes from experiments using simultaneous recordings from adjacent cortical excitatory neurons during focal stimulation of their intracortical input (Yoshimura et al., 2005). It was demonstrated that adjacent layer 2/3 pyramidal cells often do not share local excitatory input and, therefore, these neurons work relatively independent from each other. Such “fine-scale assemblies” can have important functional implications. For example, in the cat visual cortex the RF properties of pairs of nearby simple cells are seldom identical when examined in the space-time domain (DeAngelis et al., 1999; Reich et al., 2001). Such a functional diversity has been interpreted to permit efficient construction of more complex RFs from individual cell inputs. The data presented here are compatible with the above interpretations and call for further investigation to elucidate the relationship between the diversity of the neuronal network and the complex computational tasks it performs.

ACKNOWLEDGMENTS

We thank Paul R. Martin, Jason Forte, and Jonathan D. Victor for helpful discussions and comments on the article. We thank Éva Tóth for excellent technical assistance and help with the reconstructions and Róbert Magyar and Vesselin Tzvetkov for computer expertise.

LITERATURE CITED

- Adams JC. 1981. Heavy metal intensification of DAB-based HRP reaction product. *J Histochem Cytochem* 29:775–775.
- Adorján P, Levitt JB, Lund JS, Obermayer K. 1999. A model for the intracortical origin of orientation preference and tuning in macaque striate cortex. *Vis Neurosci* 16:303–318.
- Ahmed B, Anderson JC, Douglas RJ, Martin KA, Nelson JC. 1994. Polyneuronal innervation of spiny stellate neurons in cat visual cortex. *J Comp Neurol* 341:39–49.
- Albus K. 1975. A quantitative study of the projection area of the central and the paracentral visual field in area 17 of the cat. I. The precision of the topography. *Exp Brain Res* 24:159–179.
- Anderson JC, Douglas RJ, Martin KA, Nelson JC. 1994. Synaptic output of physiologically identified spiny stellate neurons in cat visual cortex. *J Comp Neurol* 341:16–24.
- Angelucci A, Levitt JB, Walton EJ, Hupe JM, Bullier J, Lund JS. 2002. Circuits for local and global signal integration in primary visual cortex. *J Neurosci* 22:8633–8646.
- Basole A, White LE, Fitzpatrick D. 2003. Mapping multiple features in the population response of visual cortex. *Nature* 424:986–990.
- Batschelet E. 1981. Circular statistics in biology. London: Academic Press.
- Ben-Shahar O, Zucker S. 2004. Geometrical computations explain projection patterns of long-range horizontal connections in visual cortex. *Neural Comput* 16:445–476.

- Ben-Yishai R, Bar-Or RL, Sompolinsky H. 1995. Theory of orientation tuning in visual cortex. *Proc Natl Acad Sci U S A* 92:3844–3848.
- Binzegger T, Douglas RJ, Martin KA. 2004. A quantitative map of the circuit of cat primary visual cortex. *J Neurosci* 24:8441–8453.
- Bishop PO. 1979. Stereopsis and the random element in the organization of the striate cortex. *Proc R Soc Lond B Biol Sci* 204:415–434.
- Blasdel GG, Salama G. 1986. Voltage-sensitive dyes reveal a modular organization in monkey striate cortex. *Nature* 321:579–585.
- Blumenfeld B, Bibitchkov D, Tsodyks M. 2006. Neural network model of the primary visual cortex: from functional architecture to lateral connectivity and back. *J Comput Neurosci* 20:219–241.
- Bonds AB. 1989. Role of inhibition in the specification of orientation selectivity of cells in the cat striate cortex. *Vis Neurosci* 2:41–55.
- Bonhoeffer T, Grinvald A. 1991. Iso-orientation domains in cat visual cortex are arranged in pinwheel-like patterns. *Nature* 353:429–431.
- Bonhoeffer T, Grinvald A. 1993. The layout of iso-orientation domains in area 18 of cat visual cortex: optical imaging reveals a pinwheel-like organization. *J Neurosci* 13:4157–4180.
- Bonhoeffer T, Grinvald A. 1996. Optical imaging based on intrinsic signals. The methodology. In: Toga AW, Mazziotta JC, editors. *Brain mapping: the methods*. San Diego: Academic Press. p 55–97.
- Bonhoeffer T, Kim DS, Malonek D, Shoham D, Grinvald A. 1995. Optical imaging of the layout of functional domains in area 17 and across the area 17/18 border in cat visual cortex. *Eur J Neurosci* 7:1973–1988.
- Bosking WH, Zhang Y, Schofield B, Fitzpatrick D. 1997. Orientation selectivity and the arrangement of horizontal connections in tree shrew striate cortex. *J Neurosci* 17:2112–2127.
- Bosking WH, Kretz R, Pucak ML, Fitzpatrick D. 2000. Functional specificity of callosal connections in tree shrew striate cortex. *J Neurosci* 20:2346–2359.
- Bosking WH, Crowley JC, Fitzpatrick D. 2002. Spatial coding of position and orientation in primary visual cortex. *Nat Neurosci* 5:874–882.
- Buzás P, Eysel UT, Kisvárdy ZF. 1998. Functional topography of single cortical cells: an intracellular approach combined with optical imaging. *Brain Res Protoc* 3:199–208.
- Buzás P, Eysel UT, Adorján P, Kisvárdy ZF. 2001. Axonal topography of cortical basket cells in relation to orientation, direction, and ocular dominance maps. *J Comp Neurol* 437:259–285.
- Buzás P, Volgushev M, Eysel UT, Kisvárdy ZF. 2003. Independence of visuotopic representation and orientation map in the visual cortex of the cat. *Eur J Neurosci* 18:957–968.
- Callaway EM, Katz LC. 1991. Effects of binocular deprivation on the development of clustered horizontal connections in cat striate cortex. *Proc Natl Acad Sci U S A* 88:745–749.
- Carreira-Perpiñán MA, Goodhill GJ. 2004. Influence of lateral connections on the structure of cortical maps. *J Neurophysiol* 92:2947–2959.
- Chisum HJ, Moosey F, Fitzpatrick D. 2003. Emergent properties of layer 2/3 neurons reflect the collinear arrangement of horizontal connections in tree shrew visual cortex. *J Neurosci* 23:2947–2960.
- Creutzfeldt OD, Kuhnt U, Benevento LA. 1974. An intracellular analysis of visual cortical neurons to moving stimuli: response in a co-operative neuronal network. *Exp Brain Res* 21:251–274.
- Cynader MS, Swindale NV, Matsubara JA. 1987. Functional topography in cat area 18. *J Neurosci* 7:1401–1413.
- Das A, Gilbert CD. 1995. Long-range horizontal connections and their role in cortical reorganization revealed by optical recording of cat primary visual cortex. *Nature* 375:780–784.
- DeAngelis GC, Ghose GM, Ohzawa I, Freeman RD. 1999. Functional micro-organization of primary visual cortex: receptive field analysis of nearby neurons. *J Neurosci* 19:4046–4064.
- Douglas RJ, Martin KA, Whitteridge D. 1991. An intracellular analysis of the visual responses of neurons in cat visual cortex. *J Physiol (Lond)* 440:659–696.
- Ernst UA, Pawelzik KR, Sahar-Pikilny C, Tsodyks MV. 2001. Intracortical origin of visual maps. *Nat Neurosci* 4:431–436.
- Erwin E, Miller KD. 1998. Correlation-based development of ocularly matched orientation and ocular dominance maps: determination of required input activities. *J Neurosci* 18:9870–9895.
- Ferster D. 1986. Orientation selectivity of synaptic potentials in neurons of cat primary visual cortex. *J Neurosci* 6:1284–1301.
- Ferster D, Miller KD. 2000. Neural mechanisms of orientation selectivity in the visual cortex. *Annu Rev Neurosci* 23:441–471.
- Gabbott PL, Martin KA, Whitteridge D. 1987. Connections between pyramidal neurons in layer 5 of cat visual cortex (area 17). *J Comp Neurol* 259:364–381.
- Gilbert CD, Wiesel TN. 1983. Clustered intrinsic connections in cat visual cortex. *J Neurosci* 3:1116–1133.
- Gilbert CD, Wiesel TN. 1989. Columnar specificity of intrinsic horizontal and corticocortical connections in cat visual cortex. *J Neurosci* 9:2432–2442.
- Grinvald A, Lieke EE, Frostig RD, Hildesheim R. 1994. Cortical point-spread function and long-range lateral interactions revealed by real-time optical imaging of macaque monkey primary visual cortex. *J Neurosci* 14:2545–2568.
- Hata Y, Tsumoto T, Sato H, Tamura H. 1991. Horizontal interactions between visual cortical neurons studied by cross-correlation analysis in the cat. *J Physiol (Lond)* 441:593–614.
- Hata Y, Tsumoto T, Sato H, Hagihara K, Tamura H. 1988. Inhibition contributes to orientation selectivity in visual cortex of cat. *Nature* 335:815–817.
- Hetherington PA, Swindale NV. 1999. Receptive field and orientation scatter studied by tetrode recordings in cat area 17. *Vis Neurosci* 16:637–652.
- Horikawa K, Armstrong WE. 1988. A versatile means of intracellular labeling: injection of biocytin and its detection with avidin conjugates. *J Neurosci Methods* 25:1–11.
- Hubel DH, Wiesel TN. 1962. Receptive fields, binocular interaction and functional architecture in the cat's visual cortex. *J Physiol (Lond)* 160:106–154.
- Hubel DH, Wiesel TN. 1963. Shape and arrangement of columns in cat's striate cortex. *J Physiol (Lond)* 165:559–568.
- Hübener M, Shoham D, Grinvald A, Bonhoeffer T. 1997. Spatial relationships among three columnar systems in cat area 17. *J Neurosci* 17: 9270–9284.
- Jones JP, Palmer LA. 1987. An evaluation of the two-dimensional Gabor filter model of simple receptive fields in cat striate cortex. *J Neurophysiol* 58:1233–1258.
- Kapadia MK, Ito M, Gilbert CD, Westheimer G. 1995. Improvement in visual sensitivity by changes in local context: parallel studies in human observers and in V1 of alert monkeys. *Neuron* 15:843–856.
- Kisvárdy ZF, Eysel UT. 1992. Cellular organization of reciprocal patchy networks in layer III of cat visual cortex (area 17). *Neuroscience* 46: 275–286.
- Kisvárdy ZF, Martin KA, Freund TF, Maglóczky Z, Whitteridge D, Somogyi P. 1986. Synaptic targets of HRP-filled layer III pyramidal cells in the cat striate cortex. *Exp Brain Res* 64:541–552.
- Kisvárdy ZF, Kim DS, Eysel UT, Bonhoeffer T. 1994. Relationship between lateral inhibitory connections and the topography of the orientation map in cat visual cortex. *Eur J Neurosci* 6:1619–1632.
- Kisvárdy ZF, Tóth É, Rausch M, Eysel UT. 1997. Orientation-specific relationship between populations of excitatory and inhibitory lateral connections in the visual cortex of the cat. *Cereb Cortex* 7:605–618.
- Koulakov AA, Chklovskii DB. 2001. Orientation preference patterns in mammalian visual cortex: a wire length minimization approach. *Neuron* 29:519–527.
- Lee BB, Albus K, Heggelund P, Hulme MJ, Creutzfeldt OD. 1977. The depth distribution of optimal stimulus orientations for neurons in cat area 17. *Exp Brain Res* 27:301–314.
- Löwel S, Singer W. 1992. Selection of intrinsic horizontal connections in the visual cortex by correlated neuronal activity. *Science* 255:209–212.
- Malach R, Amir Y, Harel M, Grinvald A. 1993. Relationship between intrinsic connections and functional architecture revealed by optical imaging and *in vivo* targeted biocytin injections in primate striate cortex. *Proc Natl Acad Sci U S A* 90:10469–10473.
- Maldonado PE, Gray CM. 1996. Heterogeneity in local distributions of orientation-selective neurons in the cat primary visual cortex. *Vis Neurosci* 13:509–516.
- Maldonado PE, Godecke I, Gray CM, Bonhoeffer T. 1997. Orientation selectivity in pinwheel centers in cat striate cortex. *Science* 276:1551–1555.
- Mante V, Carandini M. 2005. Mapping of stimulus energy in primary visual cortex. *J Neurophysiol* 94:788–798.
- McGuire BA, Gilbert CD, Rivlin PK, Wiesel TN. 1991. Targets of horizontal connections in macaque primary visual cortex. *J Comp Neurol* 305: 370–392.
- McLaughlin D, Shapley R, Shelley M, Wielaard DJ. 2000. A neuronal network model of macaque primary visual cortex (V1): orientation selectivity and dynamics in the input layer 4Calpha. *Proc Natl Acad Sci U S A* 97:8087–8092.

- Miller KD. 1994. Models of activity-dependent neural development. *Prog Brain Res* 102:303–318.
- Mitchison G, Crick F. 1982. Long axons within the striate cortex: their distribution, orientation, and patterns of connection. *Proc Natl Acad Sci U S A* 79:3661–3665.
- Monier C, Chavane F, Baudot P, Graham LJ, Fregnac Y. 2003. Orientation and direction selectivity of synaptic inputs in visual cortical neurons: a diversity of combinations produces spike tuning. *Neuron* 37:663–680.
- Mooser F, Bosking WH, Fitzpatrick D. 2004. A morphological basis for orientation tuning in primary visual cortex. *Nat Neurosci* 7:872–879.
- Pei X, Vidyasagar TR, Volgushev M, Creutzfeldt OD. 1994. Receptive field analysis and orientation selectivity of postsynaptic potentials of simple cells in cat visual cortex. *J Neurosci* 14:7130–7140.
- Peters A, Payne BR. 1993. Numerical relationships between geniculocalcarine afferents and pyramidal cell modules in cat primary visual cortex. *Cereb Cortex* 3:69–78.
- Petersen CC, Grinvald A, Sakmann B. 2003. Spatiotemporal dynamics of sensory responses in layer 2/3 of rat barrel cortex measured in vivo by voltage-sensitive dye imaging combined with whole-cell voltage recordings and neuron reconstructions. *J Neurosci* 23:1298–1309.
- Ratzlaff EH, Grinvald A. 1991. A tandem-lens epifluorescence macroscope: hundred-fold brightness advantage for wide-field imaging. *J Neurosci Methods* 36:127–137.
- Reich DS, Mechler F, Victor JD. 2001. Independent and redundant information in nearby cortical neurons. *Science* 294:2566–2568.
- Rockland KS, Lund JS. 1982. Widespread periodic intrinsic connections in the tree shrew visual cortex. *Science* 215:1532–1534.
- Roerig B, Chen B. 2002. Relationships of local inhibitory and excitatory circuits to orientation preference maps in ferret visual cortex. *Cereb Cortex* 12:187–198.
- Roerig B, Kao JP. 1999. Organization of intracortical circuits in relation to direction preference maps in ferret visual cortex. *J Neurosci* (Online) 19:RC44.
- Roerig B, Chen B, Kao JP. 2003. Different inhibitory synaptic input patterns in excitatory and inhibitory layer 4 neurons of ferret visual cortex. *Cereb Cortex* 13:350–363.
- Schmidt KE, Goebel R, Löwel S, Singer W. 1997. The perceptual grouping criterion of colinearity is reflected by anisotropies of connections in the primary visual cortex. *Eur J Neurosci* 9:1083–1089.
- Shmuel A, Grinvald A. 1996. Functional organization for direction of motion and its relationship to orientation maps in cat area 18. *J Neurosci* 16:6945–6964.
- Shmuel A, Grinvald A. 2000. Coexistence of linear zones and pinwheels within orientation maps in cat visual cortex. *Proc Natl Acad Sci U S A* 97:5568–5573.
- Sholl DA. 1955. The organization of the visual cortex of the cat. *Neurosci Lett* 170:255–260.
- Shouval HZ, Goldberg DH, Jones JP, Beckerman M, Cooper LN. 2000. Structured long-range connections can provide a scaffold for orientation maps. *J Neurosci* 20:1119–1128.
- Sincich LC, Blasdel GG. 2001. Oriented axon projections in primary visual cortex of the monkey. *J Neurosci* 21:4416–4426.
- Sirovich L, Uglesich R. 2004. The organization of orientation and spatial frequency in primary visual cortex. *Proc Natl Acad Sci U S A* 101:16941–16946.
- Somers DC, Nelson SB, Sur M. 1995. An emergent model of orientation selectivity in cat visual cortical simple cells. *J Neurosci* 15:5448–5465.
- Somogyi P, Freund TF. 1989. Immunocytochemistry and synaptic relationships of physiologically characterized HRP-filled neurons. In: Heimer L, Záborcszky L, editors. *Neuroanatomical tract-tracing methods 2: recent progress*. New York: Plenum Press. p 239–264.
- Swindale NV. 1998. Orientation tuning curves: empirical description and estimation of parameters. *Biol Cybern* 78:45–56.
- Swindale NV, Matsubara JA, Cynader MS. 1987. Surface organization of orientation and direction selectivity in cat area 18. *J Neurosci* 7:1414–1427.
- Swindale NV, Grinvald A, Shmuel A. 2003. The spatial pattern of response magnitude and selectivity for orientation and direction in cat visual cortex. *Cereb Cortex* 13:225–238.
- Takashima I, Kajiwara R, Iijima T. 2001. Voltage-sensitive dye versus intrinsic signal optical imaging: comparison of optically determined functional maps from rat barrel cortex. *Neuroreport* 12:2889–2894.
- Tieman SB, Tumosa N. 1983. [¹⁴C]2-deoxyglucose demonstration of the organization of ocular dominance in areas 17 and 18 of the normal cat. *Brain Res* 267:35–46.
- Tootell RB, Silverman MS, De Valois RL. 1981. Spatial frequency columns in primary visual cortex. *Science* 214:813–815.
- Toth LJ, Rao SC, Kim DS, Somers D, Sur M. 1996. Subthreshold facilitation and suppression in primary visual cortex revealed by intrinsic signal imaging. *Proc Natl Acad Sci U S A* 93:9869–9874.
- Ts'o DY, Gilbert CD, Wiesel TN. 1986. Relationships between horizontal interactions and functional architecture in cat striate cortex as revealed by cross-correlation analysis. *J Neurosci* 6:1160–1170.
- Tucker TR, Katz LC. 2003. Spatiotemporal patterns of excitation and inhibition evoked by the horizontal network in layer 2/3 of ferret visual cortex. *J Neurophysiol* 89:488–500.
- Tusa RJ, Palmer LA, Rosenquist AC. 1978. The retinotopic organization of area 17 (striate cortex) in the cat. *J Comp Neurol* 177:213–235.
- Tusa RJ, Rosenquist AC, Palmer LA. 1979. Retinotopic organization of areas 18 and 19 in the cat. *J Comp Neurol* 185:657–678.
- Vidyasagar TR, Pei X, Volgushev M. 1996. Multiple mechanisms underlying the orientation selectivity of visual cortical neurons. *Trends Neurosci* 19:272–277.
- Volgushev M, Pei X, Vidyasagar TR, Creutzfeldt OD. 1993. Excitation and inhibition in orientation selectivity of cat visual cortex neurons revealed by whole-cell recordings in vivo. *Vis Neurosci* 10:1151–1155.
- Volgushev M, Pernberg J, Eysel UT. 2000. Comparison of the selectivity of postsynaptic potentials and spike responses in cat visual cortex. *Eur J Neurosci* 12:257–263.
- Warren DJ, Fernandez E, Normann RA. 2001. High-resolution two-dimensional spatial mapping of cat striate cortex using a 100-microelectrode array. *Neuroscience* 105:19–31.
- Weliky M, Katz LC. 1994. Functional mapping of horizontal connections in developing ferret visual cortex: experiments and modeling. *J Neurosci* 14:7291–7305.
- Weliky M, Kandler K, Fitzpatrick D, Katz LC. 1995. Patterns of excitation and inhibition evoked by horizontal connections in visual cortex share a common relationship to orientation columns. *Neuron* 15:541–552.
- Willshaw DJ, von der Malsburg C. 1976. How patterned neural connections can be set up by self-organization. *Proc R Soc Lond B Biol Sci* 194:431–445.
- Xing J, Gerstein GL. 1996. Networks with lateral connectivity. II. Development of neuronal grouping and corresponding receptive field changes. *J Neurophysiol* 75:200–216.
- Yoshimura Y, Dantzker JL, Callaway EM. 2005. Excitatory cortical neurons form fine-scale functional networks. *Nature* 433:868–873.
- Yousef T, Bonhoeffer T, Kim DS, Eysel UT, Tóth É, Kisvárdy ZF. 1999. Orientation topography of layer 4 lateral networks revealed by optical imaging in cat visual cortex (area 18). *Eur J Neurosci* 11:4291–4308.
- Yousef T, Tóth É, Rausch M, Eysel UT, Kisvárdy ZF. 2001. Topography of orientation center connections in the primary visual cortex of the cat. *Neuroreport* 12:1693–1699.
- Yu H, Farley BJ, Jin DZ, Sur M. 2005. The coordinated mapping of visual space and response features in visual cortex. *Neuron* 47:267–280.